Complex dynamics of a nonlinear aerospace structure: experimental identification and modal interactions

J.P. Noël, L. Renson, G. Kerschen

Space Structures and Systems Laboratory
Department of Aerospace and Mechanical Engineering
University of Liège
Chemin des chevreuils 1, B-4000, Liège, Belgium

Corresponding author: J.P. Noël
Email: jp.noel@ulg.ac.be, phone: +32 4 3664854.

Abstract

Nonlinear system identification is a challenging task in view of the complexity and wide variety of nonlinear phenomena. The present paper addresses the identification of a real-life aerospace structure possessing a strongly nonlinear component with multiple mechanical stops. The complete identification procedure, from nonlinearity detection and characterization to parameter estimation, is carried out based upon experimental data. The combined use of various analysis techniques, such as the wavelet transform and the restoring force surface method, brings different perspectives to the dynamics. Specifically, the structure is shown to exhibit particularly interesting nonlinear behaviors, including jumps, modal interactions, force relaxation and chattering during impacts on the mechanical stops.

Keywords: nonlinear system identification; aerospace structure; experimental data; nonlinear modal interaction.

1 Introduction

System identification in structural dynamics, which aims at building accurate mathematical models from input and output measurements acquired on the real structure, is a discipline that has evolved considerably during the last decades. Since the early eighties, modal analysis [1, 2], which is indubitably the most popular approach to performing linear system identification of vibrating structures, has successfully embraced increasingly complex systems in a broad range of application fields. It is fair to say that modal analysis is today a mature research area, which is routinely practiced in industry using advanced and sophisticated techniques [3, 4]. However, with the continual interest in expanding the performance envelope of engineering systems, the utilization of nonlinear components is becoming more and more frequent. There thus exists a need for the development of effective system identification techniques applicable to nonlinear systems.

Nonlinear system identification is a challenging task in view of the complexity and wide variety of nonlinear phenomena. Significant progress has been enjoyed during the last fifteen years or so [5] and, to date, multi-degree-of-freedom lumped-parameter systems and continuous structures with localized nonlinearities are within reach [6, 7, 8, 9]. The identification of weak nonlinearities in more complex systems was also addressed in the recent past. In particular, Platten *et al.* successfully applied the so-called nonlinear resonance decay method [10] to an aircraft-like experimental structure that consists of a wing with two stores suspended by means of nonlinear pylons with hardening characteristics [11]. A variant of the nonlinear resonance decay method combined with a direct parameter estimation technique [12] was also proposed in [13], and provided good results in the nonlinear identification of the aileron mode of a large transport aircraft. Another methodology, limited in principle to weakly nonlinear behavior and based on frequency response measurements, was introduced by Carrella and Ewins in [14], where data collected on a complete helicopter revealed a marked softening of one vibration mode of the structure.

The identification of large-scale structures with multiple, and possibly strongly, nonlinear components nevertheless remains a distinct challenge and concentrates current research efforts. In this context, nonparametric approaches, whereby no *a priori* assumption is made regarding the type and the strength of the nonlinearities, are frequently adopted. For instance, it was lately shown that the equivalence between analytical and empirical slow flows yields an identification methodology applicable to a large class of nonlinear systems [15]. This was confirmed numerically using a rigid-wing model with aeroelastic nonlinearity [16], and experimentally on a bolted beam assembly exhibiting nonlinear friction effects [17]. The nonlinear modal properties of a similar set-up were also studied in [18], applying nonparametric techniques to measurements recorded using a scanning laser Doppler vibrometer. An interesting alternative to nonparametric modeling is the recourse to parametric models, which are generally sought by the practicing engineer because of their link with the physics. This is why the present paper addresses the parametric identification of the SmallSat spacecraft developed by EADS-Astrium, and possessing a vibration isolation device with multiple mechanical stops.

The contribution of the paper stems from an unconventional application of established

and robust analysis techniques to identify this large-scale, strongly nonlinear structure. The complete identification procedure, from nonlinearity detection and characterization to parameter estimation [5], will be achieved based upon experimental data collected during a classical spacecraft qualification campaign. Because such campaigns are constrained by the need to reduce the measurement time, no dedicated tests were performed for the purpose of this study. Typical sine-sweep driven-base data will therefore be exploited without the knowledge of the actual input force at the shaker-to-structure interface.

Throughout the paper, the combined use of analysis techniques will bring different perspectives to the dynamics. Specifically, the spacecraft will be shown to exhibit particularly interesting nonlinear behaviors, including jumps, modal interactions, force relaxation and chattering during impacts on the mechanical stops. A specific attention will be devoted to nonlinear modal interactions as their experimental evidence in the case of a complex, real-life structure is another important contribution of this work. In particular, it will be found that – potentially dangerous – nonlinear resonances between modes with non-commensurate linear frequencies are possible due to the frequency-energy dependence of nonlinear dynamics. These observations will be compared with numerical predictions obtained by applying continuation algorithms to a finite element model of the satellite structure.

The present paper starts with a detailed introduction to the SmallSat structure and its nonlinear vibration isolation device in Section 2. Low-level random data are exploited using a subspace algorithm applied to transmissibility functions to estimate the linear modal properties of the spacecraft. Nonlinearity detection is achieved in Section 3 through the visual inspection of the raw sine-sweep time series and phase-plane portraits. Restoring force plots and time-frequency spectra are then analyzed in Section 4 to gain additional insight toward accurately characterizing nonlinear behavior. Finally, a multi-degree-of-freedom formulation of the restoring force surface method, first introduced by Masri and Caughey [19], will be established in Section 5 to estimate the parameters of the nonlinear device.

2 The SmallSat spacecraft structure

The SmallSat structure was conceived by EADS-Astrium as a low-cost platform for small satellites in low earth orbits [20]. It is a monocoque tube structure which is 1.2 m in height and 1 m in width. It is composed of eight flat faces for equipment mounting purposes, creating an octagon shape, as shown in Figure 1. The octagon is manufactured using carbon-fiber-reinforced plastic by means of a filament winding process. The structure thickness is 4 mm with an additional 0.25-mm-thick skin of Kevlar applied to both the inside and outside surfaces to provide protection against debris. The top floor is an 1-m^2 sandwich aluminum panel, with 25-mm core and 1-mm skins. The interface between the spacecraft and the launch vehicle is achieved via four aluminum brackets located around cut-outs at the base of the structure. The total mass including the interface brackets is around 64 kg.

[Figure 1 about here.]

The spacecraft structure supports a dummy telescope mounted on a baseplate through a tripod; its mass is around 140 kg. The dummy telescope plate is connected to the SmallSat top floor by three shock attenuators, termed shock attenuation systems for spacecraft and adaptor (SASSAs) [21], whose dynamic behavior may exhibit nonlinearity. Besides, as depicted in Figure 2 (a), a support bracket connects to one of the eight walls the so-called wheel elastomer mounting system (WEMS) device which is loaded with an 8-kg dummy inertia wheel. The WEMS device acts as a mechanical filter which mitigates high-frequency disturbances coming from the inertia wheel through the presence of a soft elastomeric interface between its mobile part, *i.e.* the inertia wheel and a supporting metallic cross, and its fixed part, *i.e.* the bracket and by extension the spacecraft. Moreover, the WEMS incorporates eight mechanical stops, covered with a thin layer of elastomer, and designed to limit the axial and lateral motions of the inertia wheel during launch, which gives rise to strongly nonlinear dynamic phenomena.

Figure 2 (b) presents a simplified, yet relevant, modeling of the WEMS device where the inertia wheel, owing to its important rigidity, is seen as a point mass. The four nonlinear connections (NCs) between the WEMS mobile and fixed parts are labeled NC $1-4$. Each NC possesses a trilinear spring in the axial direction (elastomer in traction/compression plus two stops), a bilinear spring in the radial direction (elastomer in shear plus one stop), and a linear spring in the third direction (elastomer in shear). The stiffness and damping properties of the WEMS were estimated during experiments carried out by EADS-Astrium at subsystem level (see Table 1), and will serve as reference values in this study. For confidentiality, stiffness coefficients and clearances are given through adimensionalised quantities.

[Figure 2 about here.]

[Table 1 about here.]

Low-level random data were acquired throughout the test campaign, specifically between each qualification run, to monitor the integrity of the structure. This was performed considering axial white-noise excitations filtered in 5 – 100 Hz and driven via a base acceleration of 0.001 g^2/Hz. As they are not recommended by the space testing standards, high-level random excitations were not applied. The low-level time series are exploited herein to identify the linear modal properties of the spacecraft, utilizing transmissibility functions (TFs) as no force measurement was available at the shaker-to-structure interface. The TFs measured on the dummy inertia wheel and telescope in the X, Y and Z directions are plotted in Figure 3, given a reference accelerometer located on the shaking table. One remarks that the large bandwidths of the resonance peaks reveal the high damping induced by the elastomeric components in the system. The ordinary coherence functions corresponding to the axial TFs of Figures 3 (e – f) are also depicted in Figures 4 (a – b), respectively. They are both seen to be close to unity for most of the excited frequencies and deteriorate beyond 80 Hz due to poor signal-to-noise ratio. This proves that the structure can be assumed to behave linearly at this low input level and, in turn, that the analysis of the TFs can yield a reliable identification of its linear modal properties. This analysis is carried out using the frequency-domain subspace algorithm derived in reference [22]. The resulting estimates of the resonance frequencies and damping ratios of the spacecraft are given in Table 2. One notes that the two significant dips observed in Figure 4 (a) around 10 and 45 Hz can be attributed to the presence of modes 1, 5 and 6 in the corresponding intervals. The estimated damping ratios also confirm the presence of high damping in the system.

[Table 2 about here.]

The actual qualification test campaign consisted of swept-sine base excitations applied to the spacecraft for different amplitude levels, sweep rates and directions, as prescribed by the testing standards established by the European Space Agency (ESA) [23]. Two specific data sets measured under 0.6 g and 1 g axial loadings and for positive sweep rates of 2 and 4 octaves per minute, respectively, are exploited in the present work for nonlinear system identification. For conciseness, their analysis is focused in the next sections on the frequency range between 5 and 15 Hz, *i.e.* the vicinity of the first mode of vibration of the structure. The associated spacecraft motion is depicted in Figure 5 through the modal coordinates of the inertia wheel and telescope in the X, Y and Z directions. This motion consists mainly in a swing oscillation of the inertia wheel around Y-axis.

[Figure 3 about here.]

[Figure 4 about here.]

[Figure 5 about here.]

3 Detection of nonlinearity

Nonlinearity detection is the first step of the parametric identification process, and basically boils down to seeking departures from linear theory predictions. In this regard, stepped- and swept-sine excitations are particularly convenient because, if linear, the structure is known to generate a pure sine wave in output, and distortions may be detected without requiring complicated post-processing. Various other concepts for the analysis of linear systems do not directly apply to nonlinear theory, and may therefore serve in principle as detection tools. However, they generally require high-level random measurements that are not available in this study, as is the case for the test for homogeneity of frequency response functions and ordinary coherences, or the subspace angle technique [24].

3.1 Envelope-based analysis of the raw time series

Nonlinear distortions in response to sine excitations can sometimes be such that a mere visual inspection of the raw time series is sufficient to reveal nonlinear behavior. To this end, the relative displacements across NC 1 along Z-axis measured at 0.6 g and 1 g are plotted in Figures 6 (a – b), respectively, versus sweep frequency. Note that the excitation frequency is an exponential function of time with a rate, which is the derivative of frequency with respect to time, expressed in octaves per minute [23]. Given the knowledge of the sweep rate, this definition enables the conversion from time to sweep frequency throughout the paper. Note also that the measured accelerations were integrated twice using the trapezium rule and then high-pass filtered to obtain displacement signals [25]. For confidentiality, relative displacements and velocities are adimensionalised throughout the paper.

The first observation is the absence of proportionality between the time responses in Figures 6 (a – b). This is especially visible for negative displacements where the maximum amplitude reached at 0.6 g and 1 g is almost unchanged. This violates the principle of superposition, a cornerstone of the linear theory. The location of the resonance in amplitude in the two graphs can also be seen to be shifted towards higher frequencies, from 8.3 to 9 Hz as the level is increased from 0.6 to 1 g. One further remarks the clear skewness and nonsmoothness of the envelope of oscillations in Figure 6 (b), which exhibits a sudden transition from large to small amplitudes of vibration, referred to as a jump phenomenon. This envelope also presents a significant asymmetry entailing larger amplitudes of motion in positive displacement, and a discontinuity in slope for negative displacements around 7.5 Hz.

By contrast, the envelope of response at 0.6 g shows no evidence of nonlinear distortion. However, analyzing the response in the vicinity of resonance, *i.e.* in the 8.1 – 8.4 Hz interval, as presented in Figure 6 (c), highlights the presence of harmonics in the time series. A similar inspection at 1 g, depicted in Figure 6 (d) in 8.4 – 8.7 Hz, reveals much more significant harmonics and a limitation of the amplitude of motion in negative displacement resulting in the aforementioned asymmetry of the response.

[Figure 6 about here.]

3.2 Phase-plane diagram

An under-utilized but useful means of revealing harmonic distortions is a phase-plane diagram, where the system's trajectory draws an ellipse in the case of a pure sine wave in output. The relative displacements of Figures 6 (c – d) are plotted versus the corresponding relative velocities to generate phase-plane trajectories in Figures 7 (a – b), respectively. The detection of harmonics at 0.6 g is now straightforward, and the activation of a strongly nonlinear regime of motion is also confirmed at 1 g.

A meaningful representation of the nonlinear jump phenomenon observed in Figure 6 (b) can also be achieved in the phase plane. This phenomenon stems from the intrinsic property of a nonlinear system to possess multiple stable solutions of its equations of motion, with co-existing basins of attraction. This competing co-existence may result in "jumps" between solutions for small perturbations of the system, in particular small variations of the forcing frequency. Figure 7 (c) depicts the phase-plane trajectory corresponding to Figure 6 (b) in the interval from 9 to 10 Hz, and parametrized by the excitation frequency as a color map. This reveals a sudden transition at 9.4 Hz from a nonlinear to a linear regime of motion, *i.e.* from a high- to a low-amplitude solution of the equations of motion.

[Figure 7 about here.]

In summary of the nonlinearity detection step, all these results highlight multiple symptoms of the activation of nonlinear dynamics at 1 g, namely the loss of superposition principle, the shift of the resonance frequency, the jump phenomenon, the asymmetry and discontinuity of the response envelope, and the presence of significant harmonics. The diagnosis is similar at 0.6 g where nonlinear distortions, though being much less significant, were made evident in a distorted phase-plane trajectory.

4 Characterization of nonlinearity

Nonlinearity characterization is the second step of the parametric identification process, and amounts to selecting appropriate functional forms to represent the nonlinearities in the system. Characterization is of paramount importance, as the success of the third step of the process, *i.e.* the estimation of model parameters, is conditional upon a precise understanding of the nonlinear mechanisms involved. It is also a very challenging step because the physical phenomena that entail nonlinearity are numerous and may result in plethora of dynamic behaviors.

4.1 Visual inspection and histogram

Beyond detection, the visual inspection of the time series can help gain insight into nonlinear behavior. The existence of a discontinuity in the envelope of oscillation in Figure 6 (b) results from the nonsmooth nature of the nonlinearity, and the existence of a clearance in the system. The location of the discontinuity yields a direct estimation of this clearance at around -1. The modification of the slope of the envelope also translates a substantial increase of stiffness, which is confirmed by the shift of the resonance towards higher frequencies in Figures 6 (a – b), and by the amplitude-limiting effect visible in Figure 6 (d). Finally, the asymmetry observed in the response can be explained by the prestress applied to the elastomer plots by gravity, which implies a smaller clearance in the – Z direction.

A particularly meaningful representation of the measured time series for clearance estimation is a histogram. This is plotted in Figures 8 (a – b) for the relative displacements of Figures 6 (a – b), respectively. The accumulation of samples in the left-hand tail of the double-peak-shaped distribution typical of sine waves, which is another manifestation of the asymmetry of the WEMS device, leads to a consistent estimation of the NC 1 negative clearance at 1. Note that a more accurate estimation of NC 1 and NC 2 clearances will be realized in Section 5.

[Figure 8 about here.]

4.2 Restoring force surface plots

The restoring force surface (RFS) method, covered in detail in the textbook [12], serves commonly as a parameter estimation technique, as in Section 5 of the present paper. This section introduces an unconventional use of the RFS method for nonlinearity characterization purposes, relying exclusively on measured signals. The starting point is Newton's law of dynamics written for a specific degree of freedom (DOF) located next to a nonlinear structural component, namely

$$\sum_{n=1}^{N} m_{i,n}\,\ddot{q}_n + f_i(\mathbf{q},\dot{\mathbf{q}}) = p_i \tag{1}$$

where i is the DOF of interest, N the number of DOFs in the system, $m_{i,j}$ the mass matrix elements, $\mathbf{q}$, $\dot{\mathbf{q}}$ and $\ddot{\mathbf{q}}$ the displacement, velocity and acceleration vectors, respectively, $\mathbf{f}$ the restoring force vector encompassing elastic and dissipative effects, and $\mathbf{p}$ the external force vector. The key idea of the approach is to discard in Equation (1) all the inertia and restoring force contributions that are not related to the nonlinear component, as they are generally either unknown, *e.g.* the coupling inertia coefficients, or not measured, *e.g.* the rotational DOFs. If we denote by j another measured DOF located across the nonlinear connection, Equation (1) is therefore approximated by

$$m_{i,i}\,\ddot{q}_i + f_i(q_i - q_j, \dot{q}_i - \dot{q}_j) \approx p_i. \tag{2}$$

If no force is applied to DOF i, a simple rearrangement leads to

$$f_i(q_i - q_j, \dot{q}_i - \dot{q}_j) \approx -m_{i,i}\,\ddot{q}_i. \tag{3}$$

Equation (3) shows that the restoring force of the nonlinear connection is approximately proportional to the acceleration at DOF i. Hence, by simply representing the acceleration signal, with a negative sign, measured at one side of the nonlinear connection as a function of the relative displacement and velocity across this connection, the nonlinearities can be conveniently visualized, and an adequate mathematical model for their description can then be selected. This methodology was already successfully applied to the characterization of the nonlinearities at the wing tip of the MS-760 Morane Saulnier aircraft [26], and in the wing-to-payload interfaces of an F-16 aircraft [27].

To visualize the elastic nonlinearities of the WEMS device, a cross section along the axis where the velocity is zero of the restoring force surface defined by the triplets $(q_{i,k} - q_{j,k}, \dot{q}_{i,k} - \dot{q}_{j,k}, -\ddot{q}_{i,k})$, where k refers to the k-th sampled instant, can be drawn. Figures 9 (a – b) show the plots corresponding to NC 1 at 0.6 g and 1 g, respectively. These figures are particularly useful as they reaffirm the nonsmooth and asymmetric nature of the nonlinearities in the system, and the estimation of the – Z clearance at around 1. The restoring force curve at 1 g also reveals the activation of the + Z stop, beyond a relative displacement of about 1.5. In Section 2, the SASSA isolators were also mentioned as possible sources of nonlinear behavior. Figures 9 (c – e) depict the nonlinearities across the three SASSA connections in the Z direction at 1 g. As suspected, they exhibit a weak nonlinearity, which is however not further investigated in favor of the much stronger nonlinearities of the WEMS device.

[Figure 9 about here.]

4.3 Time-frequency analysis using the wavelet transform

The Fourier transform (FT), which maps a time-domain signal $x(t)$ onto its frequency-domain representation $X(\omega)$, is defined as

$$X(\omega) = \int_{-\infty}^{\infty} x(t)\, e^{-j\omega t}\, dt\,. \tag{4}$$

Though it is widely used in structural dynamics for various purposes, the FT fails to capture nonstationary effects. In this regard, an improvement of the classical FT is the short-time Fourier transform (STFT). The signal to be analyzed is first multiplied by a window $w(t-\tau)$, which is nonzero for only a short period of time. The FT of the signal is then calculated as the window $w(t-\tau)$ is slid along the time axis, resulting in a more general time-dependent representation $X(\omega,\tau)$ of the spectrum of the signal

$$X(\omega,\tau)=\int_{-\infty}^{\infty} x(t)\,w(t-\tau)\,e^{-j\omega t}\,dt\,. \tag{5}$$

The inherent limitation of the STFT is that the window length is not adjustable, and a wide (narrow) window thus gives good (poor) frequency resolution but poor (good) time resolution. This fixed resolution of the STFT can be addressed using more sophisticated time-frequency analysis methodologies, such as the wavelet transform (WT). Unlike the STFT, the WT involves a windowing strategy with variable-sized regions:

$$X(a,b)=\frac{1}{\sqrt{a}}\int_{-\infty}^{\infty} x(t)\,\psi\left(\frac{t-b}{a}\right)\,dt \tag{6}$$

where ψ is referred to as the mother wavelet. Parameter b, similarly to τ, locates the observation window in the time domain, and a contracts or expands the window depending upon the frequency components of $x(t)$. This adaptability makes the WT one of the most suitable tools for interpreting harmonics generated by nonlinear systems in response to swept-sine excitations [28]. The Morlet mother wavelet, which is a Gaussian-windowed complex exponential, is exploited herein for its versatility.

The wavelet amplitudes of the relative displacements of Figures 6 (a – b) are displayed in logarithmic scaling in Figures 10 (a – b), respectively. At 0.6 g, the appearance of wideband frequency components around 8.5 Hz, including even harmonics, confirms the activation of a nonsmooth nonlinearity in the neighborhood of the resonance and the existence of an asymmetry in the system. Figure 10 (b) shows that, at 1 g, the nonlinearity is activated over a wider sweep frequency interval. Nonsmooth effects are also found to be stronger as indicated by the relative importance of the harmonics in the response. The disappearance of the wideband content at 1 g can be seen to coincide closely with the jump phenomenon observed in Figure 6 (b). One should also point out that impurities in the input sine wave turn into weak harmonics visible throughout the spectra, but hence not attributable to nonlinearity. Similarly, electrical noise is responsible for polluting frequency lines around 50 Hz.

In summary, the nonlinearity characterization step reveals that an accurate representation of the WEMS nonlinear behavior should account for combined nonsmooth and asymmetric effects. This leads us to select a trilinear model with dissimilar clearances for the nonlinearity, as presented in Figure 11. No characterization of damping was attempted in this section as the scope of this work is focused on the identification of the nonlinear dynamics introduced by the WEMS mechanical stops. Moreover, the understanding of dissipation mechanisms is particularly challenging, and would certainly deserve specific test data other than the sine sweeps available herein. One therefore opts for a simple linear damping model for the elastomer components of the WEMS, even if it will be shown in Section 5.2 that they may exhibit more complex, time-dependent characteristics.

[Figure 10 about here.]

[Figure 11 about here.]

4.4 Evidence of nonlinear modal interactions

The WT can evidence another salient feature of nonlinear systems that has no counterpart in linear theory, namely modal interactions between well-separated modes. These interactions were extensively studied in the technical literature [29, 30, 31], but they were so far rarely reported in the case of a real-life structure. To reveal nonlinear modal interactions in the SmallSat dynamics, Figure 12 (a) depicts the wavelet amplitude of the acceleration measured at NC 4 in the Z direction over 5 – 35 Hz. Compared to the two wavelets represented in Figure 10 (a – b), a linear scale is used herein to focus on the most significant frequency components in the time series. The excitation frequency is clearly seen throughout the wavelet, but higher harmonic components of at least comparable amplitude are also visible. In particular, a significant level of response, encircled in Figure 12 (a), is observed around 60 Hz for sweep frequencies just below 30 Hz. This corresponds to a 2:1 interaction between two internally resonant modes of the structure, namely mode 3, which involves an out-of-phase motion of the inertia wheel and the WEMS bracket, and mode 7, which consists in an axial motion of the telescope supporting panel. The existence of a 2:1 interaction between modes 3 and 7 is confirmed in Figure 12 (b) where the raw acceleration signal measured at the center of the instrument panel is plotted at 0.1 g and 1 g. A high amplitude response at 1 g is observed between 20 and 30 Hz, which can be confidently attributed to a nonlinear resonance as no linear mode of the panel is located in this interval. One also remarks the presence of two resonances around 46 and 56 Hz, as predicted by the linear modal analysis carried out in Section 2. At the 0.1 g excitation level for which the satellite behaves linearly, there is no sign of the 2:1 modal interaction, proving that it is an inherently nonlinear phenomenon activated for sufficiently large energies.

[Figure 12 about here.]

[Figure 13 about here.]

[Figure 14 about here.]

[Figure 15 about here.]

Unlike what is frequently discussed in the literature [29], the ratio of the linear natural frequencies of modes 3 and 7 is not an integer, it is around 2.5 (see Table 2). However, the frequency of nonlinear modes may vary according to the excitation level. This is clearly visible in Figure 13 where the acceleration measured at NC 3 is plotted at 0.1 g and 1

g. At 0.1 g, the linear resonance frequencies of modes 2 and 3 identified in Section 2 are retrieved around 20.3 and 23 Hz, whereas they are seen to be shifted up to 24 and 29 Hz at 1 g, respectively. This means that a 2:1 ratio between modes 3 and 7 can still be realized due to the energy dependence of nonlinear modes. Indeed, the frequency of mode 3 increases rapidly as soon as nonlinearity is activated (as it will be confirmed in Figure 14), whereas the frequency of mode 7 remains unchanged as it involves no WEMS motion. This is therefore the experimental evidence of an interaction between nonlinear modes with noncommensurate linear frequencies. It should also be stressed that this 2:1 modal interaction may jeopardize the integrity of the structure as it is accompanied by an energy transfer from a local mode of the spacecraft with low effective mass, *i.e.* mode 3, to a global mode with high effective mass, *i.e.* mode 7. In addition, the time series at 1 g in Figure 12 (b) shows that the nonlinear resonance involving the instrument panel is associated with larger accelerations (*i.e.*, 100 m/s^2) than the linear resonance of the panel (*i.e.*, 80 m/s^2). Finally, the 2:1 interaction is not an isolated phenomenon as other internal resonances, such as a 5:2 interaction between mode 2 and mode 7 and a 4:1 interaction between modes 2 and 9, can also be noticed in Figure 12 (a). This implies that important, and potentially dangerous, dynamic phenomena can be missed when ignoring nonlinearity.

Interactions between nonlinear modes can be reliably predicted using numerical continuation algorithms [31, 32]. To this end, a finite element model of the SmallSat satellite was developed [33] and is used in the present study to compute its nonlinear normal modes (NNMs) and frequencies. Figure 14 depicts the frequency-energy plot (FEP) of mode 3. An NNM, which is a periodic solution of the underlying Hamiltonian system, is represented by a point in the FEP, drawn at a frequency corresponding to the minimal period of the periodic motion and at an energy equal to the conserved total energy during the motion. A branch depicted by a solid line represents the complete frequency-energy dependence of the considered mode. The FEP of mode 3 has a complex structure. It is formed by a main backbone to which several "tongues" are attached. At low energies, no mechanical stop is activated, and the NNM frequency remains constant. Its modal shape drawn at point A in Figure 14 is identical to the corresponding normal mode of the underlying linear system. Beyond a certain energy threshold, mechanical stops are activated, and the NNM frequency rapidly increases due to the nonsmooth nature of the WEMS nonlinearities. The tongues correspond to nonlinear modal interactions during which one harmonic component of mode 3 excites another mode of the structure [31]. Specifically, a 2:1 interaction can be distinguished in Figure 14. The modal shape depicted at its right end shows that a transition from a local mode involving the WEMS device to a more global mode of the instrument panel, located between 57 and 58 Hz, takes place. The excitation of this higher-frequency mode is possible thanks to the second harmonics generated by the nonlinear behavior of mode 3. This is therefore the clear numerical confirmation of the experimental observation in Figures 12 (a – b). Note that the low-level frequencies of modes 3 and 7 play no role in the ability of the finite element model to predict their nonlinear interaction at high level. Bringing the linear frequencies of the model in very close quantitative agreement with the experimental estimates given in Table 2 was therefore not attempted. This absence of a formal model updating process explains the discrepancy between the experimental and numerical linear frequencies

of mode 3, equal to 22.45 Hz and 28.75 Hz, respectively. Note also that other modal interactions, namely 3:1, 9:1 and 26:1, are predicted by the continuation algorithm but are not further investigated in this work.

Figure 15 eventually shows that an additional 2:1 experimental modal interaction can be evidenced using the WT, for instance by analyzing the acceleration measured at NC 4 in the Y direction. This modal interaction is interesting because, at this sensor, the only visible frequency component is 45 Hz despite the fact that the excitation frequency is 22.5 Hz.

5 Parameter estimation in the presence of nonlinearity

Based on the choice made in Section 4 to use trilinear functional forms to characterize the WEMS elastic behavior together with linear damping properties, the last step toward the establishment of a nonlinear model with good predictive capabilities is the estimation of the associated parameters, *i.e.* the clearances, stiffness and damping coefficients. This is arguably the most difficult step in the identification process, but also the one that conveys the most valuable information about the system under test. Quite surprisingly, a review of the technical literature about parameter estimation [5] reveals that base-sine excitations have so far received little attention in the nonlinear system identification community. This is manifestly because a measure of the force is a common requirement of most existing techniques, as is the case for nonlinear auto-regressive [34], frequency-domain feedback [35], reverse path [36, 37] or subspace methods [38, 39]. It turns out from this survey that the RFS method is one of the only approaches compatible with unmeasured base-sine excitations.

Though it was shown to extend to multi-DOF systems [40], the utilization of the RFS method for parameter estimation is in general limited to small-scale structures, since the starting point of the approach is a rigorous writing of Newton's second law as discussed in Section 4.2. For instance, an impacting beam was studied in [41] as a single-DOF system through a band-limited excitation centered on its first natural frequency. The nonlinear identification of an automotive shock absorber that was constrained to move in only one direction to justify a single-DOF assumption is also described in [42]. Al-Hadid and Wright addressed a T-beam structure with well-separated bending and torsion modes in [43].

5.1 Multi-degree-of-freedom RFS-based methodology

In this section, it is demonstrated that the equations of motion of the WEMS mobile part, *i.e.* the dummy inertia wheel and its metallic cross-shaped support, can be formulated explicitly by asserting that it behaves as a rigid body. The dynamics of a rigid body is known to obey 6 scalar equations, namely 3 equations describing the translation of its center of gravity, and 3 equations governing the rotation of the body around the center of gravity. One herein concentrates on the translation along Z-axis of the center of gravity

of WEMS mobile part. Under the rigidity assumption, its kinetic energy T_z thus writes

$$T_z = \frac{1}{2}\, m\, \dot{z}_{CoG}^{\,2} \tag{7}$$

where m is the mass of the WEMS mobile part estimated at 8.75 kg and $\dot{z}_{CoG}$ the Z-velocity of its center of gravity. This latter quantity can simply be evaluated as the mean of the axial velocities of two opposite NCs, namely

$$\dot{z}_{CoG} = \frac{\dot{z}_1 + \dot{z}_2}{2}. \tag{8}$$

The potential energy V_z associated with the trilinear stiffness forces in the system is formed as

$$V_z = V_{NC\,1}(z_1) + V_{NC\,2}(z_2) \tag{9}$$

where the contributions related to NC 3 and NC 4 are neglected as they involve considerably lower displacements. This results from the swing motion of the WEMS around Y-axis observed in the frequency band of interest (see Figure 5 in Section 2). Similarly, damping forces in NC 3 and NC 4 are neglected in the writing of the dissipation function D_z, *i.e.*

$$D_z = \frac{1}{2}\, c_1\, \dot{z}_1^{\,2} + \frac{1}{2}\, c_2\, \dot{z}_2^{\,2} \tag{10}$$

were c_1 and c_2 are the linear damping coefficients of the NC 1 and NC 2 elastomer plots, respectively. Note that in the definition of the potential energy and dissipation function in Equations (9) and (10), respectively, it is assumed that there exists no coupling term between the restoring forces at NC 1 and NC 2, so that their contributions can be separated. The axial equation of motion of the WEMS mobile part can finally be deduced from Lagrange's equation

$$\frac{d}{dt}\left(\frac{\partial T_z}{\partial \dot{z}}\right) - \frac{\partial T_z}{\partial z} + \frac{\partial V_z}{\partial z} + \frac{\partial D_z}{\partial \dot{z}} = 0. \tag{11}$$

Therefore, plugging Equations (7), (8), (9) and (10) into Equation (11) yields

$$m\, \frac{\ddot{z}_1 + \ddot{z}_2}{2} + f_{NC\,1}(z_1) + c_1\, \dot{z}_1 + f_{NC\,2}(z_2) + c_2\, \dot{z}_2 = 0 \tag{12}$$

where $f_{NC\,1}$ and $f_{NC\,2}$ are the trilinear stiffness forces.

It is interesting to point out that the rigidity assumption imposes geometrical constraints onto the possible motion of the WEMS. Hence, if we denote by $\vec{v}_{12}$ and $\vec{v}_{34}$ the vectors joining opposite NCs, we have

$$\begin{cases} d(v_{12})/dt = d(v_{34})/dt = 0 \\ \vec{v}_{12} \cdot \vec{v}_{34} = 0 \\ v_{12,X}/2 = v_{34,X}/2 \\ v_{12,Y}/2 = v_{34,Y}/2 \\ v_{12,Z}/2 = v_{34,Z}/2 \end{cases} \tag{13}$$

where $v_{12,X}$, $v_{12,Y}$ and $v_{12,Z}$ are the projections of $\vec{v}_{12}$ onto X-, Y- and Z-axis, respectively, and similarly for $\vec{v}_{34}$. Considering the metallic cross in Figure 2 (b), these constraints express the invariability of the length of its two arms, their orthogonality and their common

midpoints, respectively. Beyond this geometrical interpretation, they provide a means of verifying quantitatively the rigidity of the WEMS mobile part. To this end, Figure 16 represents the deviations in percent from these six scalar constraint relationships, observed as the excitation frequency increases at 1 g level. In general, they are well satisfied, and orthogonality is even found to be exactly verified, as intuitively guessed. The largest errors occur in the X direction, being however limited to less than 5 % at resonance. This confirms that the WEMS motion in the 5 – 15 Hz band is predominantly a swing oscillation entailing impacts onto the NC 1 and NC 2 stops.

[Figure 16 about here.]

The restoring force surfaces constructed via Equation (12) at NC 1 and NC 2 given the triplets $(z_1,\ \dot{z}_1,\ f_{NC\,1} + c_1\ \dot{z}_1)$ and $(z_2,\ \dot{z}_2,\ f_{NC\,2} + c_2\ \dot{z}_2)$, respectively, can now be fitted using a trilinear model in stiffness and a linear model in damping. Curve-fitting results are given in Table 3, and were computed in the 8.5 – 9 Hz interval in which the system's first resonance is located. The damping coefficients of the elastomer plots are found to be much larger than their reference value of 63 Ns/m, but are prone to significant uncertainty as they were computed from a limited number of low-displacement samples. The stiffness curves extracted as cross sections of the corresponding restoring force surfaces are plotted in Figures 17 (a – b), together with the fitted trilinear models. The calculated coefficients show that the stiffnesses of the elastomer plots and mechanical stops match well their reference values of 8 and 100, respectively, considering that no asymmetry was introduced in the reference model. Impacts are also found to be comparatively softer for positive displacements.

Moreover, one observes the existence of an even stiffness contribution in the curve in Figure 17 (a), which is attributed to gravity and is in line with the WEMS asymmetry clearly evidenced in Figures 6 (d), 8 (b) and 9 (b). This term essentially originates from an initial displacement of the system from its gravity-free equilibrium position [44]. Nevertheless, because of its marginal significance in the characterization of the nonlinearity, no even term was incorporated in the WEMS stiffness model. It should also be noticed that there appears no gravity-induced trend in Figure 17 (b). This is because the bracket hardly bends at NC 2 and is thus locally close to its gravity-free equilibrium position.

Finally, a comparison between the measured and reconstructed restoring forces across NC 1 and NC 2 is shown in Figures 18 (a – b), respectively, for sweep frequencies in 8.6 – 8.7 Hz. The agreement between the two curves is satisfactory in view of the complexity of the time series. In particular, the fundamental frequency of vibration is correctly retrieved by the model and the increase of stiffness for positive displacements in Figure 18 (a) is also well represented. However, for negative displacements, the reconstructed curves fail to capture the complete behavior of the system during impacts. This discrepancy, which can be attributed to viscoelastic effects introduced by the elastomer components of the WEMS and contact chattering, is further analyzed in the next section. One also notes that the identification of the NC 3 and NC 4 parameters could be achieved using a similar procedure, but this would require additional testing of the spacecraft as the corresponding mechanical stops were not activated during the measurement campaign considered herein.

[Table 3 about here.]

[Figure 17 about here.]

[Figure 18 about here.]

5.2 Internal force relaxation and chattering

The restoring force surface derived from Equation (12) at NC 1 is shown in Figure 19, and exhibits an asymmetry with respect to the zero-velocity axis. Specifically, for negative displacements, the appearance of large force values, signaling impacts on the mechanical stop, dies out as velocity goes from negative to positive values. This suggests a viscoelastic behavior of the elastomer components in the system, namely internal force relaxation. This phenomenon is better perceived in Figures 20 (a – b) where the relative displacement and restoring force corresponding to Figure 19 are displayed versus sweep frequency. The joint analysis of the two graphs clearly demonstrates the decrease of the internal force for constant negative displacements around -1. This motivated us to construct the stiffness curves in Figures 17 (a – b) as cross sections of the corresponding restoring force surfaces for velocities lower than -0.07 m/s, *i.e.* prior to the initiation of force relaxation.

[Figure 19 about here.]

[Figure 20 about here.]

Furthermore, it can be estimated that a single relaxation cycle lasts 0.025 s, which can appear to be extremely fast, but may result from the high speed of loading (typically 0.15 m/s and acceleration of about 100 m/s^2), the prestress in the filtering plots and the limited thickness of the elastomer layer hit during impacts. Prestress combined with speed of loading could also explain why relaxation is not manifest for positive velocities. It is also interesting to note that the displacement in Figure 20 (a) is not rigorously constant within the relaxation regions, but exhibits rapid bounces. These bounces are interpreted as a contact chattering phenomenon [45, 46] triggered by the conflict between prestress and restoring forces. Chattering explains why relaxation occurs through oscillations in Figure 20 (b) and not as a monotonic decrease. Moreover, in the simple Maxwell model for viscoelasticity, the stress is found to decrease exponentially with time at constant strain. The decay envelopes in the relaxation regions in the same figure confirm this prediction. One finally presents in Figure 21 the locus of the minima and maxima of the oscillating force decays for 6 successive relaxation regions. Minima and maxima are depicted through squares and circles, respectively, and a typical force relaxation pattern is also superimposed in this figure. The squares and circles are both found to form clusters, which indicates that the relaxation behavior observed in Figure 20 (b) is in fact generic during impacts on the mechanical stops.

[Figure 21 about here.]

6 Conclusions

The first objective of this paper was to address the experimental identification of a real-life aerospace structure exhibiting strongly nonlinear dynamics due to multiple mechanical stops. For this purpose, no dedicated tests were performed, but rather typical sine-sweep data collected during a qualification campaign of the spacecraft were exploited. The complete progression through nonlinearity detection, characterization and parameter estimation was carried out by means of several existing analysis techniques. Their combined utilization allowed to achieve an accurate modeling of the structure, including the estimation of the clearances and nonlinear stiffness properties of the nonlinear components.

The second objective of the paper was to demonstrate that the complex dynamics that can be obtained during numerical simulations of nonlinear systems with low dimensionality can also be observed in experimental conditions commonly endured by engineering structures in industry. This includes intrinsically nonlinear phenomena such as jumps and modal interactions, but also force relaxation and chattering during impacts on the mechanical stops. In particular, the evidence of modal interactions between modes with noncommensurate linear frequencies is interesting as they were so far rarely reported in the technical literature in the case of real-life, strongly nonlinear systems. They were also successfully correlated with predictions obtained by continuation algorithms applied to a finite element model of the spacecraft.

Acknowledgments

This paper was prepared in the framework of the European Space Agency (ESA) Technology Research Programme study “Advancement of Mechanical Verification Methods for Non-linear Spacecraft Structures (NOLISS)” (ESA contract No.21359/08/NL/SFe). Experimental data were measured by EADS-Astrium and LMS International. The authors also thank Astrium SAS for sharing information about the SmallSat spacecraft.

The authors J.P. Noël and L. Renson are Research Fellows (FRIA fellowship) of the *Fonds de la Recherche Scientifique – FNRS* which is gratefully acknowledged.

References

[1] D. J. Ewins, Modal Testing: Theory, Practice and Application, Research Studies Press LTD, Hertfordshire, 2000.

[2] N. M. M. Maia, and J. M. M. Silva, Theoretical and Experimental Modal Analysis, Research Studies Press LTD, Taunton, 1997.

[3] P. Van Overschee, and B. De Moor, Subspace Identification for Linear Systems: Theory, Implementation, Applications, Kluwer Academic Publishers, Dordrecht, 1996.

[4] B. Peeters, H. Van Der Auweraer, and P. Guillaume, The PolyMAX frequency domain method: a new standard for modal parameter estimation?, *Journal of Shock and Vibration* 11 (2004), 395-409.

[5] G. Kerschen, K. Worden, A. F. Vakakis, and J.C. Golinval, Past, present and future of nonlinear system identification in structural dynamics, *Mechanical Systems and Signal Processing* 20 (2006), 505-592.

[6] G. Dimitriadis, Experimental validation of the constant level method for the identification of non-linear multi-degree-of-freedom systems, *Journal of Sound and Vibration* 258(5) (2002), 829-845.

[7] M. B. Özer, H. N. Özgüven, and T. J. Royston, Identification of structural nonlinearities using describing functions and the Sherman-Morrison method, *Mechanical Systems and Signal Processing* 23 (2009), 30-44.

[8] S.T. Trickey, L.N. Virgin, and E.H. Dowell, The stability of limit-cycle oscillations in a nonlinear aeroelastic system, *Proceedings of the Royal Society of London Series A* 458 (2002), 2203-2226.

[9] G. Kerschen, V. Lenaerts, and J.C. Golinval, Identification of a continuous structure with a geometrical non-linearity, part I: conditioned reverse path method, *Journal of Sound and Vibration* 262 (2003), 889-906.

[10] M. F. Platten, J. R. Wright, G. Dimitriadis, and J. E. Cooper, Identification of multi-degree of freedom non-linear systems using an extended modal space model, *Mechanical Systems and Signal Processing* 23(1) (2009), 8-29.

[11] M. F. Platten, J. R. Wright, J. E. Cooper, and G. Dimitriadis, Identification of a nonlinear wing structure using an extended modal model, *Journal of Aircraft* 46(5) (2009), 1614-1626.

[12] K. Worden, and G. R. Tomlinson, Nonlinearity in Structural Dynamics: Detection, Identification and Modelling, Institute of Physics Publishing, Bristol and Philadelphia, 2001.

[13] U. Fuellekrug, and D. Goege, Identification of weak non-linearities within complex aerospace structures, *Aerospace Science and Technology* 23(1) (2012), 53-62.

[14] A. Carrella, and D. J. Ewins, Identifying and quantifying structural nonlinearities in engineering application from measured frequency response functions, *Mechanical Systems and Signal Processing* 25 (2011), 1011-1027.

[15] Y. S. Lee, S. Tsakirtzis, A. F. Vakakis, L. A. Bergman, and D. M. McFarland, A time-domain nonlinear system identification method based on multiscale dynamic partitions, *Meccanica* 46(4) (2011), 625-649.

[16] Y. S. Lee, A. F. Vakakis, D. M. McFarland, and L. A. Bergman, Non-linear system identification of the dynamics of aeroelastic instability suppression based on targeted energy transfers, *Aeronautical Journal* 114 (2010), 61-82.

[17] M. Eriten, M. Kurt, G. Luo, D. M. McFarland, L. A. Bergman, and A. F. Vakakis, Nonlinear system identification of frictional effects in a beam with a bolted joint connection, *Mechanical Systems and Signal Processing* 39 (2013), 245-264.

[18] M. W. Sracic, M. S. Allen, and H. Sumali, Identifying the modal properties of nonlinear structures using measured free response time histories from a scanning laser Doppler vibrometer, *In the proceedings of the International Modal Analysis Conference (IMAC) XIX*, Jacksonville, FL, 2012.

[19] S. F. Masri, and T. K. Caughey, A nonparametric identification technique for nonlinear dynamic problems, *Journal of Applied Mechanics* 46 (1979), 433-447.

[20] A. G. Russell, Thick skin, faceted, CFRP, monocoque tube structure for smallsats, *In the proceedings of the European Conference on Spacecraft Structures, Materials and Mechanical Testing*, Noordwijk, The Netherlands, 2000.

[21] P. Camarasa, and S. Kiryenko, Shock attenuation system for spacecraft and adaptor (SASSA), *In the proceedings of the European Conference on Spacecraft Structures, Materials and Mechanical Testing*, Toulouse, France, 2009.

[22] T. McKelvey, H. Akçay, and L. Ljung, Subspace-based multivariable system identification from frequency response data, *IEEE Transactions on Automatic Control* 41 (1996), 960-979.

[23] A. Calvi, and N. Roy (Eds.), Spacecraft mechanical loads analysis handbook, *ESA Requirements and Standards Division*, 2013.

[24] A. Hot, G. Kerschen, E. Foltête, and S. Cogan, Detection and quantification of nonlinear structural behavior using principal component analysis, *Mechanical Systems and Signal Processing* 26 (2012), 104-116.

[25] K. Worden, Data processing and experiment design for the restoring force surface method, Part I: integration and differentiation of measured time data, *Mechanical Systems and Signal Processing* 4 (1990), 295-319.

[26] G. Kerschen, M. Peeters, J.C. Golinval, and C. Stephan, Nonlinear modal analysis of a full-scale aircraft, *Journal of Aircraft* 50(5) (2013), 1409-1419.

[27] J.P. Noël, L. Renson, G. Kerschen, B. Peeters, S. Manzato, and J. Debille , Nonlinear dynamic analysis of an F-16 aircraft using GVT data, *In the proceedings of the International Forum on Aeroelasticity and Structural Dynamics*, Bristol, UK, 2013.

[28] W. J. Staszewski, Analysis of non-linear systems using wavelets, *Proceedings of the Institution of Mechanical Engineers Part C – Journal of Mechanical Engineering Science* 214(11) (2000), 1339-1353.

[29] A. H. Nayfeh, Nonlinear Interactions: Analytical, Computational and Experimental Methods, Wiley-Interscience, New-York, 2000.

[30] M. E. King, A. F. Vakakis, An energy-based approach to computing resonant nonlinear normal modes, *Journal of Applied Mechanics* 63 (1995), 810-819.

[31] G. Kerschen, M. Peeters, J.C. Golinval, and A. F. Vakakis, Nonlinear normal modes, Part I: A useful framework for the structural dynamicist, *Mechanical Systems and Signal Processing* 23 (2009), 170-194.

[32] M. Peeters, R. Viguié, G. Sérandour, G. Kerschen, and J.C. Golinval, Nonlinear normal modes, Part II: Toward a practical computation using numerical continuation techniques, *Mechanical Systems and Signal Processing* 23 (2009), 195-216.

[33] L. Renson, J.P. Noël, G. Kerschen, and A. Newerla, Nonlinear modal analysis of the SmallSat spacecraft, *In the proceedings of the European Conference on Spacecraft Structures, Materials and Environmental Testing*, Noordwijk, The Netherlands, 2012.

[34] I. J. Leontaritis, and S. A. Billings, Input-output parametric models for nonlinear systems, Part I: deterministic nonlinear systems, *International Journal of Control* 41 (1985), 303-328.

[35] D. E. Adams, and R. J. Allemang, A frequency domain method for estimating the parameters of a non-linear structural dynamic model through feedback, *Mechanical Systems and Signal Processing* 14(4) (2000), 637-656.

[36] C. M. Richards, and R. Singh, Identification of multi-degree-of-freedom non-linear systems under random excitations by the "reverse path" spectral method, *Journal of Sound and Vibration* 213 (1998), 673-708.

[37] P. Muhamad, N. D. Sims, and K. Worden, On the orthogonalised reverse path method for nonlinear system identification, *Journal of Sound and Vibration* 331 (2012), 4488-4503.

[38] S. Marchesiello, and L. Garibaldi, A time domain approach for identifying nonlinear vibrating structures by subspace methods, *Mechanical Systems and Signal Processing* 22 (2008), 81-101.

[39] J.P. Noël, and G. Kerschen, Frequency-domain subspace identification for nonlinear mechanical systems, *Mechanical Systems and Signal Processing* 40 (2013), 707-717.

[40] S. F. Masri, H. Sassi, and T. K. Caughey, A nonparametric identification of nearly arbitrary nonlinear systems, *Journal of Applied Mechanics*, 49 (1982), 619-628.

[41] G. Kerschen, J.C. Golinval, and K. Worden, Theoretical and experimental identification of a non-linear beam, *Journal of Sound and Vibration*, 244(4) (2001), 597-613.

[42] K. Worden, D. Hickey, M. Haroon, and D. E. Adams, Nonlinear system identification of automotive dampers: A time and frequency-domain analysis, *Mechanical Systems and Signal Processing*, 23 (2009), 104-126.

[43] M. A. Al-Hadid, and J. R. Wright, Application of the force-state mapping approach to the identification of non-linear systems, *Mechanical Systems and Signal Processing*, 4 (1990), 463-482.

[44] J. L. Huang, R. K. L. Su, Y. Y. Lee, and S. H. Chen, Nonlinear vibration of a curved beam under uniform base harmonic excitation with quadratic and cubic nonlinearities, *Journal of Sound and Vibration*, 330 (2011), 5151-5164.

[45] C. C. Lo, A cantilever beam chattering against a stop, *Journal of Sound and Vibration*, 69(2) (1980), 245-255.

[46] D. J. Wagg, Periodic sticking motion in a two-degree-of-freedom impact oscillator, *International Journal of Non-linear Mechanics*, 40 (2005), 1076-1087.

List of Figures

1 SmallSat spacecraft equipped with an inertia wheel supported by the WEMS device and a dummy telescope connected to the main structure by the SASSA isolators. 24

2 WEMS device. (a) Detailed description of the WEMS components; (b) simplified modeling of the WEMS mobile part considering the inertia wheel as a point mass. The linear and nonlinear connections between the WEMS mobile and fixed parts are signaled by squares and circles, respectively. Throughout the paper, lateral motions of the WEMS device correspond to X- and Y-axis, and axial motion refers to Z-axis. 25

3 Transmissibility functions computed using low-level random data (0.001 g^2/Hz) in the X (first row), Y (second row) and Z (last row) directions. Left column: dummy inertia wheel; right column: dummy telescope. 26

4 Ordinary coherence functions computed using low-level random data (0.001 g^2/Hz) in the Z direction. (a) Dummy inertia wheel; (b) dummy telescope. 27

5 First mode of vibration of the spacecraft described through the modal coordinates of the dummy inertia wheel and telescope in the X, Y and Z directions. 28

6 Nonlinearity detection at 0.6 g (left column) and 1 g (right column). (a – b) Envelope-based analysis; (c – d) close-up of the displacement signals. . . 29

7 Nonlinearity detection using phase-plane diagrams at (a) 0.6 g and (b) 1 g; (c) representation of the nonlinear jump phenomenon observed in Figure 6 (b) in the phase plane parametrized by the excitation frequency. . 30

8 Nonlinearity characterization via histograms of the time series. (a) 0.6 g; (b) 1 g. 31

9 Nonlinearity characterization of the WEMS device (top row) and of the three SASSA isolators (bottom row) using the restoring force surface method. (a) 0.6 g; (b – e) 1 g. 32

10 Nonlinearity characterization through the WT amplitude of the relative displacement measured across NC 1. (a) 0.6 g; (b) 1 g. 33

11 Trilinear model with dissimilar clearances selected to represent the WEMS elastic nonlinearities. The negative and positive clearances are denoted a_- and a_+, respectively; the linear and nonlinear stiffness coefficients in negative and positive displacement are denoted k, k_- and k_+, respectively. 34

12 (a) Evidence of nonlinear modal interactions using the WT calculated at NC 4 in the Z direction, and presented in 5 – 35 Hz in linear scaling. A 2:1 modal interaction between modes 3 and 7 is encircled; (b) confirmation of the existence of the 2:1 modal interaction through the raw acceleration measured at the center of the instrument panel at 0.1 g (in blue) and 1 g (in black). 35

13 Acceleration measured at NC 3 at 0.1 g (in blue) and 1 g (in black). 36

14 FEP of mode 3 computed using a continuation algorithm. The energy transfer between modes 3 and 7 is made visible through the mode shapes depicted at low level (A) and at the tip of the resonance tongue (B). 37

15 Evidence of another nonlinear modal interactions using the WT at NC 4 in the Y direction, presented in 5 – 35 Hz in linear scaling. 38

16 Verification of the geometrical conditions of rigidity at 1 g (in percent). (a – b) Length invariability; (c) orthogonality; (d – f) midpoint coincidence. . 39

17 WEMS nonlinear stiffness curves constructed based upon Equation (12) (in black) and compared with the fitted trilinear models (in blue). (a) NC 1; (b) NC 2. 40

18 Comparison between the measured (in black) and reconstructed (in blue) restoring forces versus sweep frequency. (a) NC 1; (b) NC 2. 41

19 Restoring force surface measured at NC 1, and associated with the stiffness curve displayed in Figure 17 (a). 42

20 Internal force relaxation and chattering evidenced through the comparison of the (a) relative displacement and (b) restoring force at NC 1 plotted versus sweep frequency. 43

21 Locus of the minima and maxima of the oscillating force decays for 6 successive relaxation regions depicted through squares and circles, respectively. A typical force relaxation pattern is also superimposed to the clusters of minima and maxima. 44

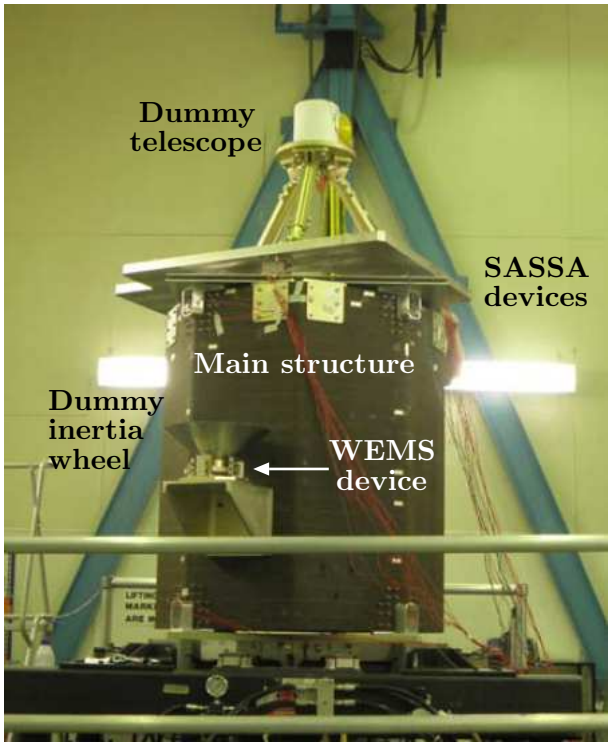

Figure 1: SmallSat spacecraft equipped with an inertia wheel supported by the WEMS device and a dummy telescope connected to the main structure by the SASSA isolators.

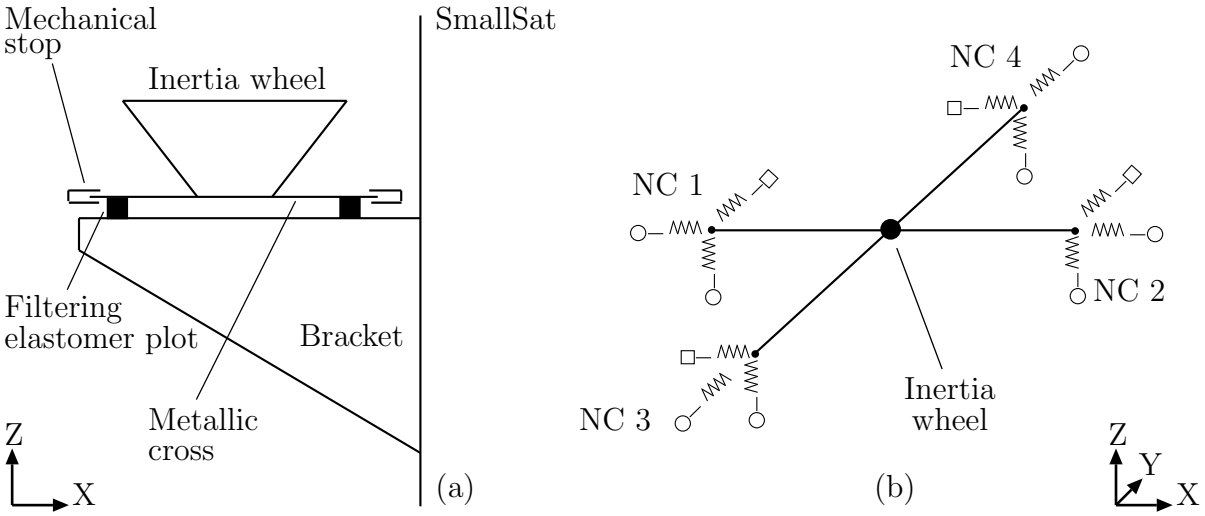

Figure 2: WEMS device. (a) Detailed description of the WEMS components; (b) simplified modeling of the WEMS mobile part considering the inertia wheel as a point mass. The linear and nonlinear connections between the WEMS mobile and fixed parts are signaled by squares and circles, respectively. Throughout the paper, lateral motions of the WEMS device correspond to X- and Y-axis, and axial motion refers to Z-axis.

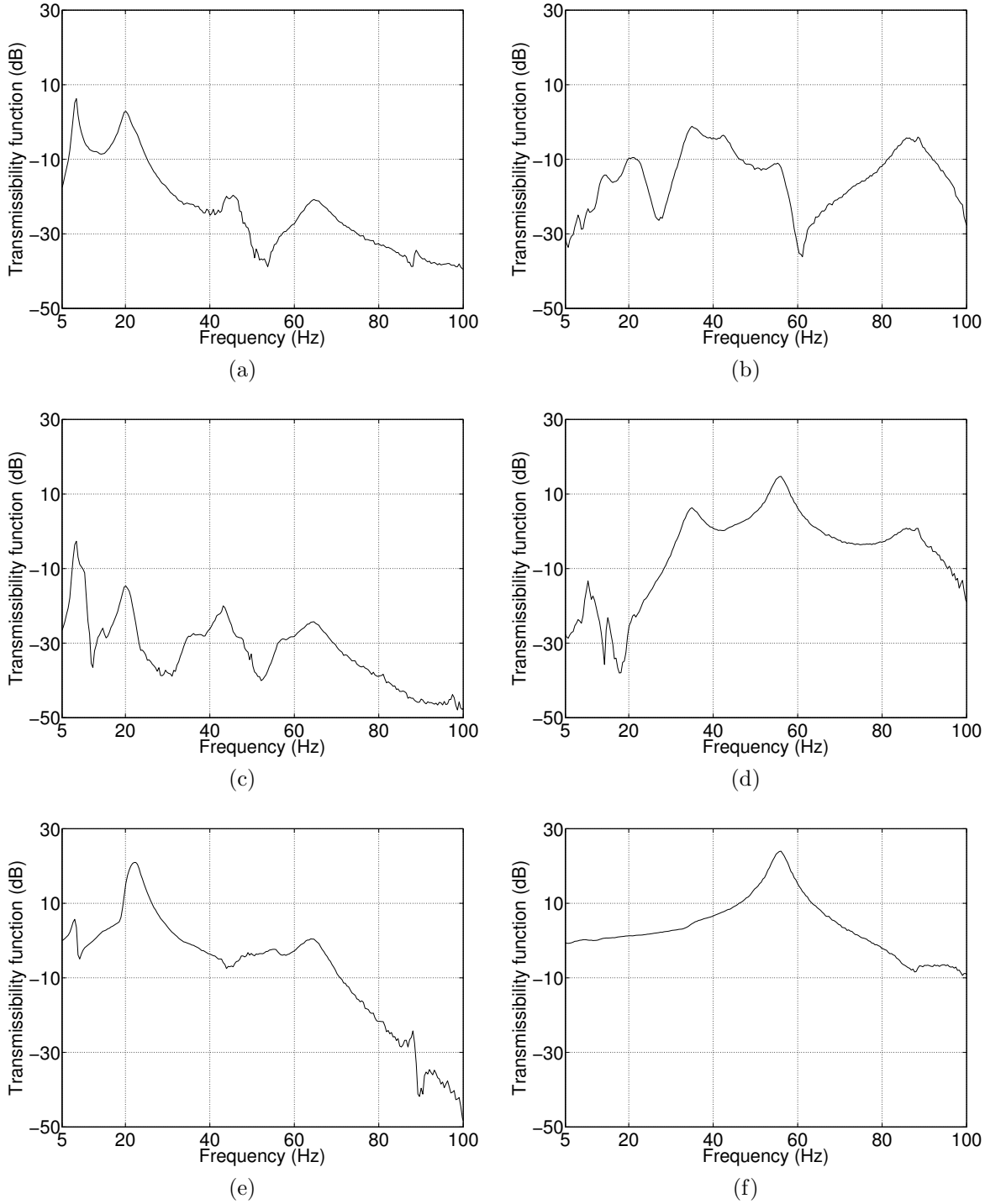

Figure 3: Transmissibility functions computed using low-level random data ($0.001\ g^2/Hz$) in the X (first row), Y (second row) and Z (last row) directions. Left column: dummy inertia wheel; right column: dummy telescope.

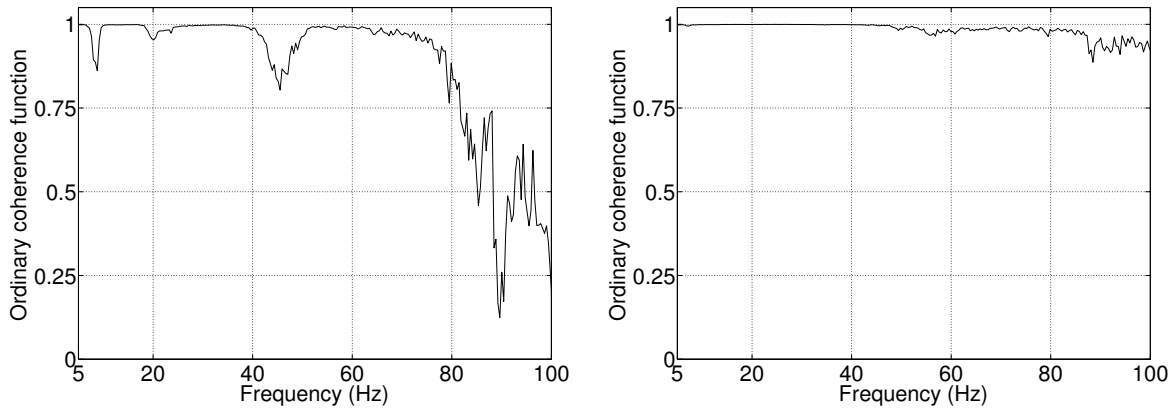

(a) (b)

Figure 4: Ordinary coherence functions computed using low-level random data (0.001 g^2/Hz) in the Z direction. (a) Dummy inertia wheel; (b) dummy telescope.

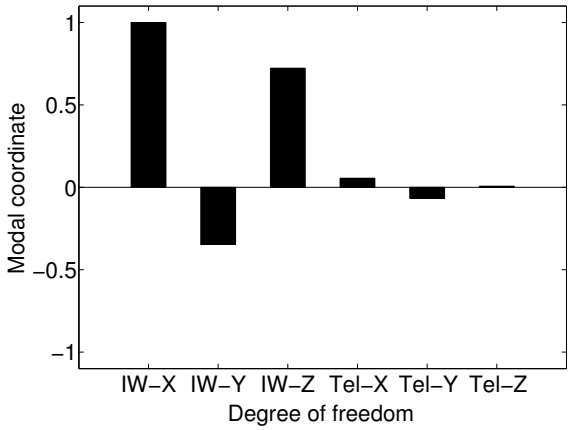

Figure 5: First mode of vibration of the spacecraft described through the modal coordinates of the dummy inertia wheel and telescope in the X, Y and Z directions.

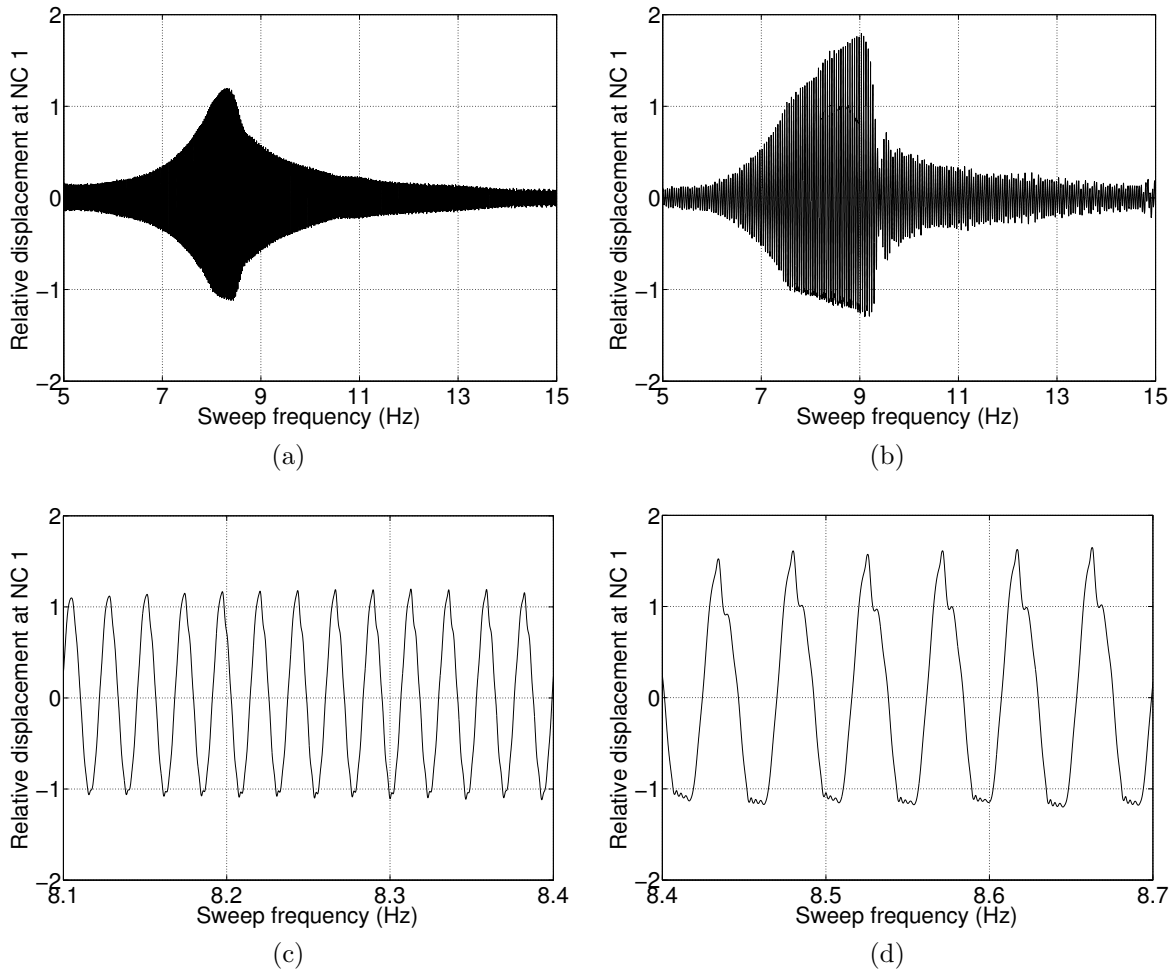

Figure 6: Nonlinearity detection at 0.6 g (left column) and 1 g (right column). (a – b) Envelope-based analysis; (c – d) close-up of the displacement signals.

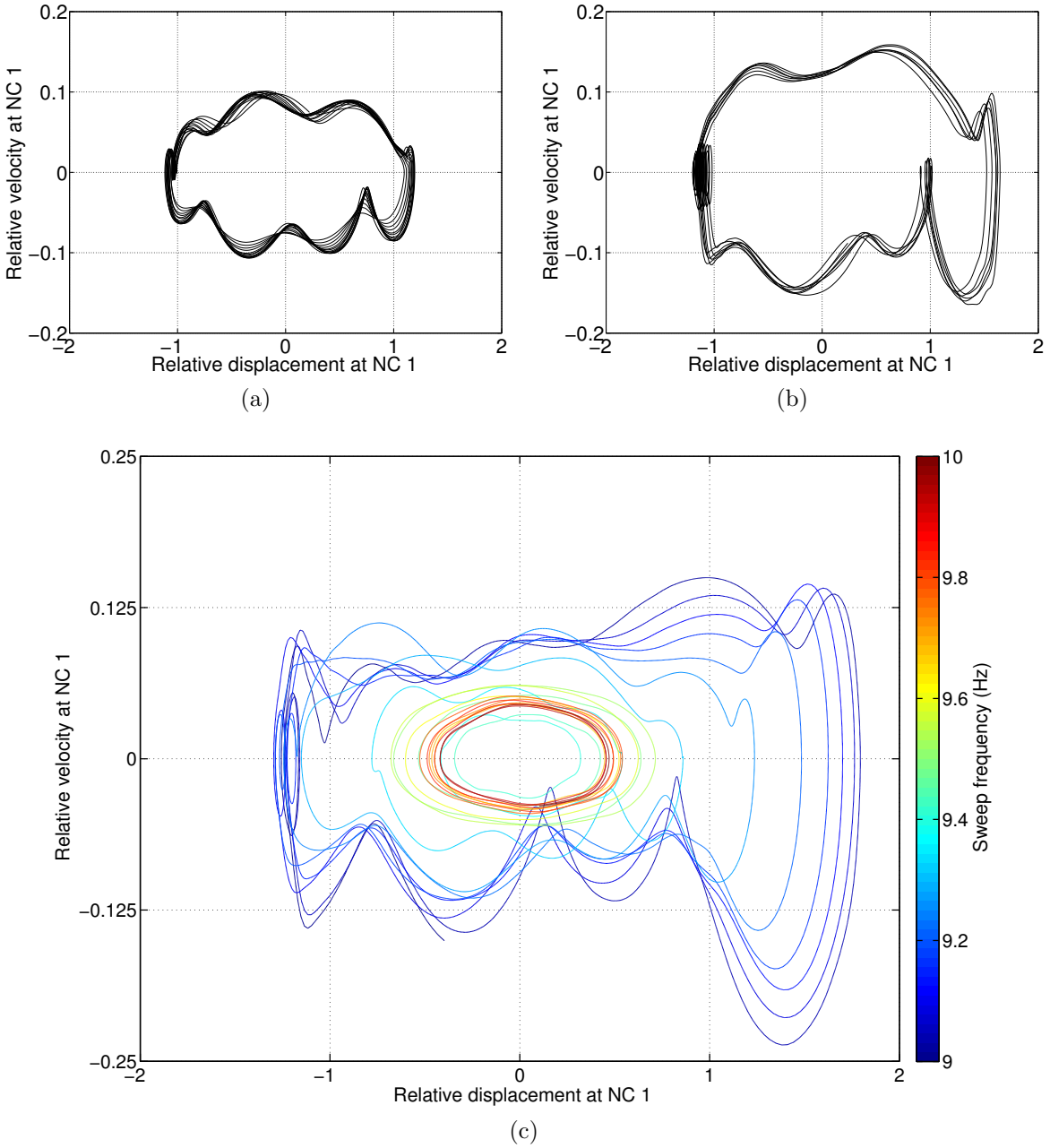

Figure 7: Nonlinearity detection using phase-plane diagrams at (a) 0.6 g and (b) 1 g; (c) representation of the nonlinear jump phenomenon observed in Figure 6 (b) in the phase plane parametrized by the excitation frequency.

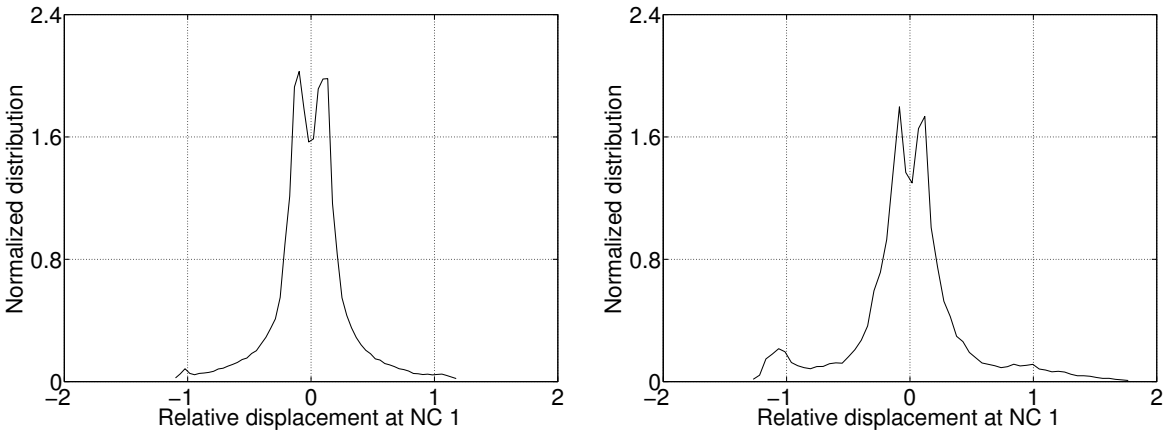

(a) (b)

Figure 8: Nonlinearity characterization via histograms of the time series. (a) 0.6 g; (b) 1 g.

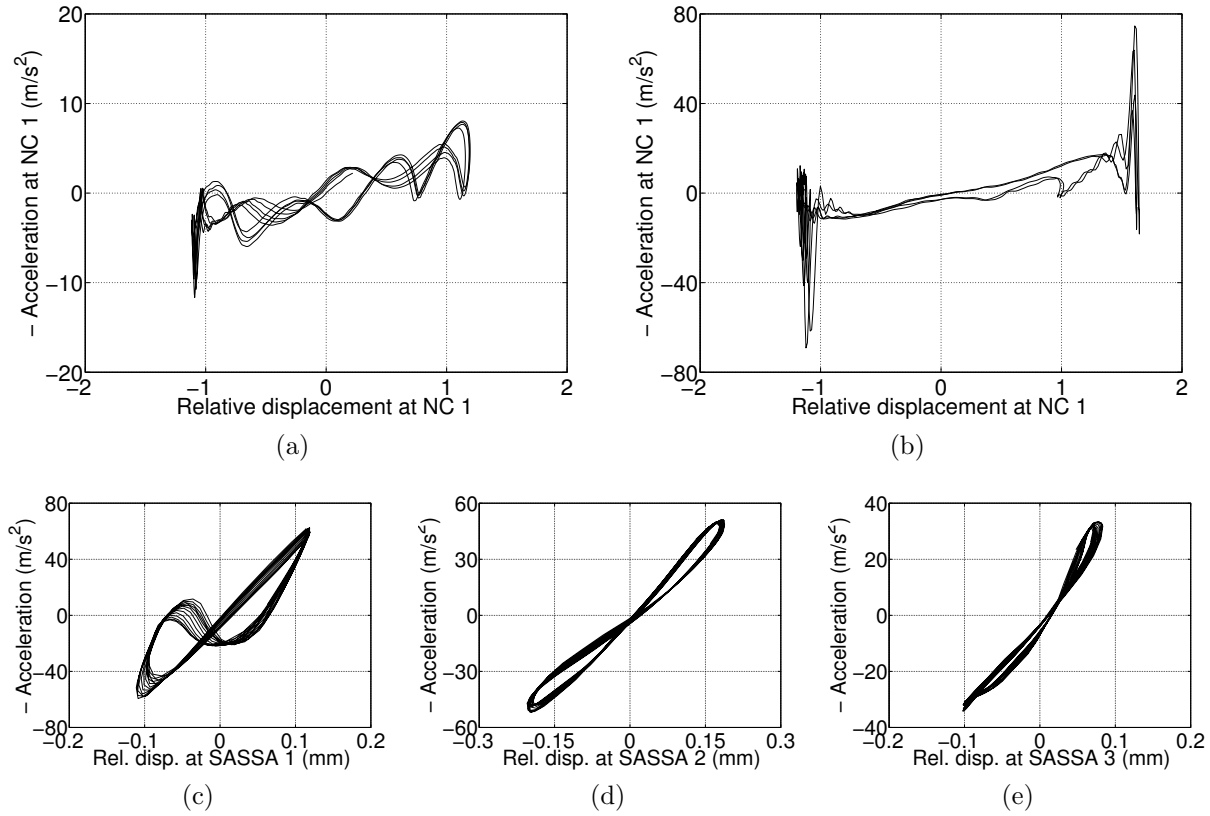

Figure 9: Nonlinearity characterization of the WEMS device (top row) and of the three SASSA isolators (bottom row) using the restoring force surface method. (a) 0.6 g; (b – e) 1 g.

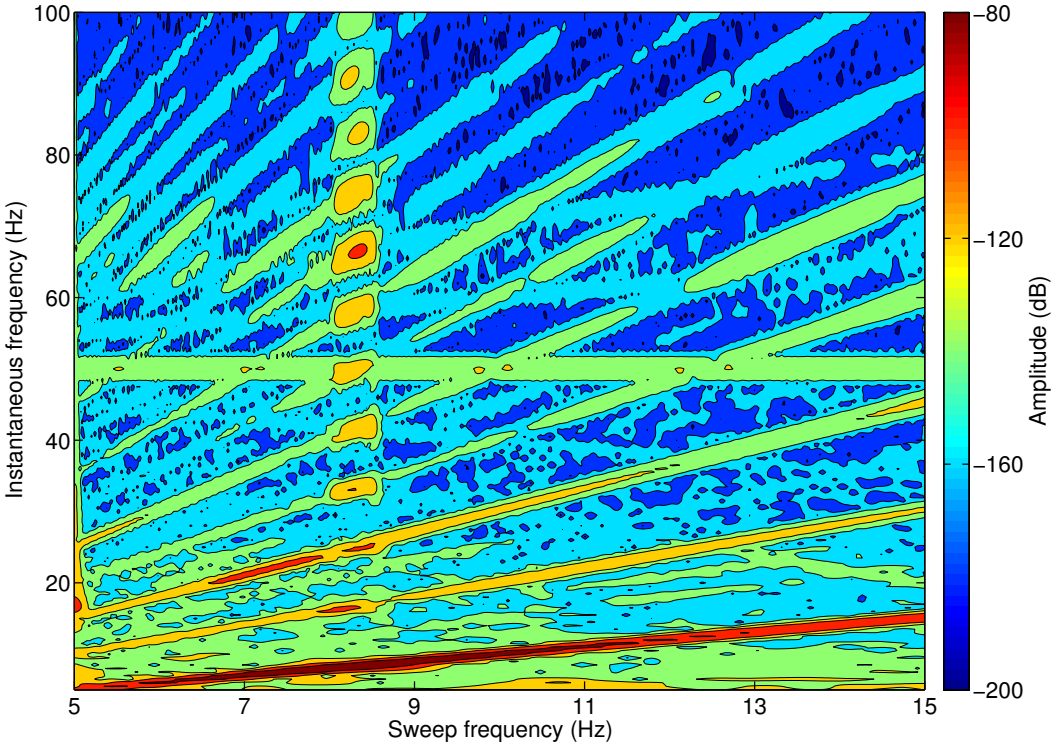

(a)

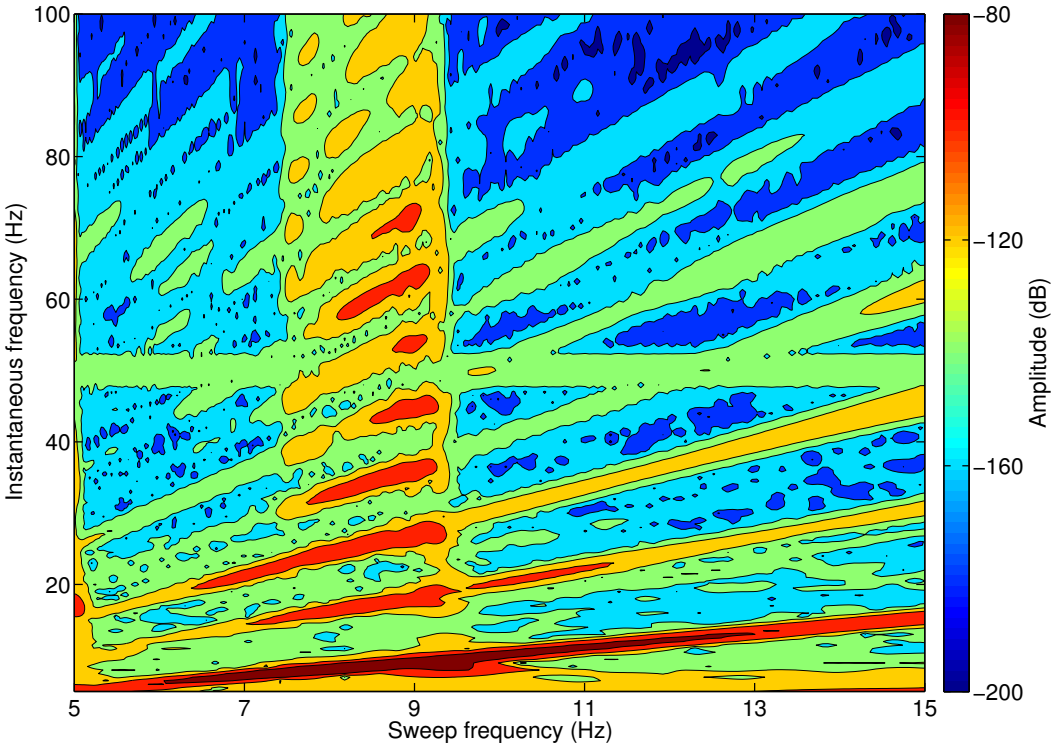

(b)

Figure 10: Nonlinearity characterization through the WT amplitude of the relative displacement measured across NC 1. (a) 0.6 g; (b) 1 g.

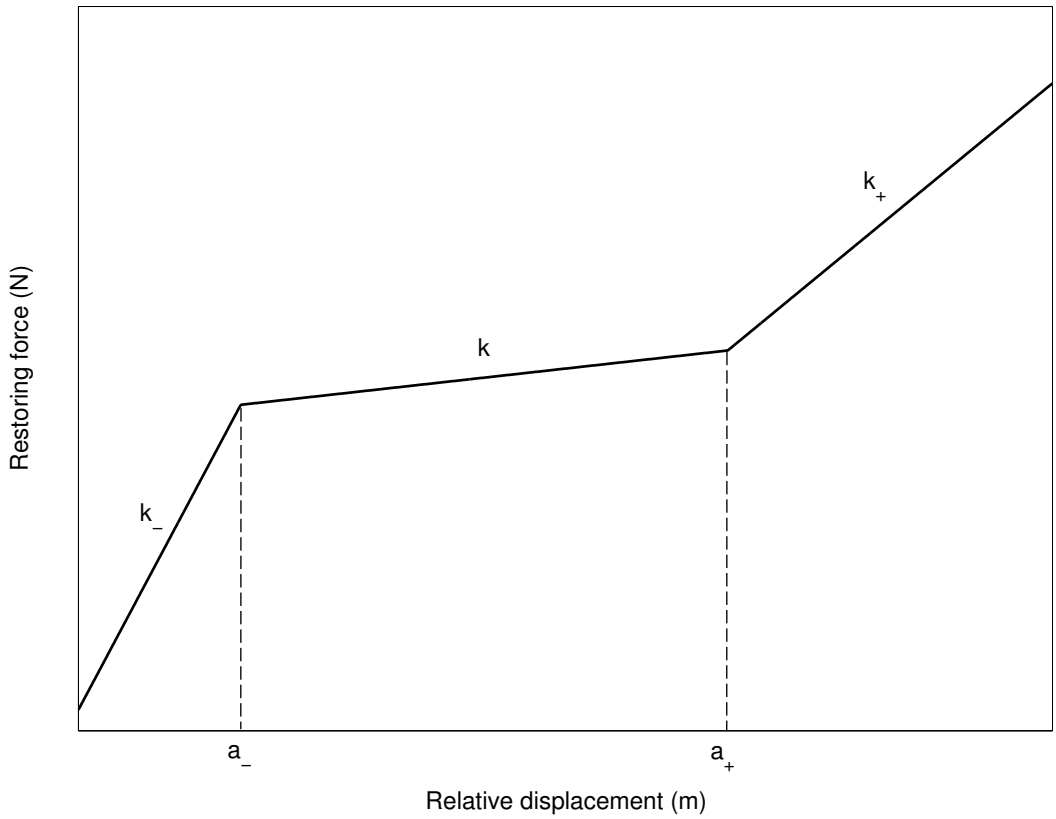

Figure 11: Trilinear model with dissimilar clearances selected to represent the WEMS elastic nonlinearities. The negative and positive clearances are denoted a_- and a_+, respectively; the linear and nonlinear stiffness coefficients in negative and positive displacement are denoted k, k_- and k_+, respectively.

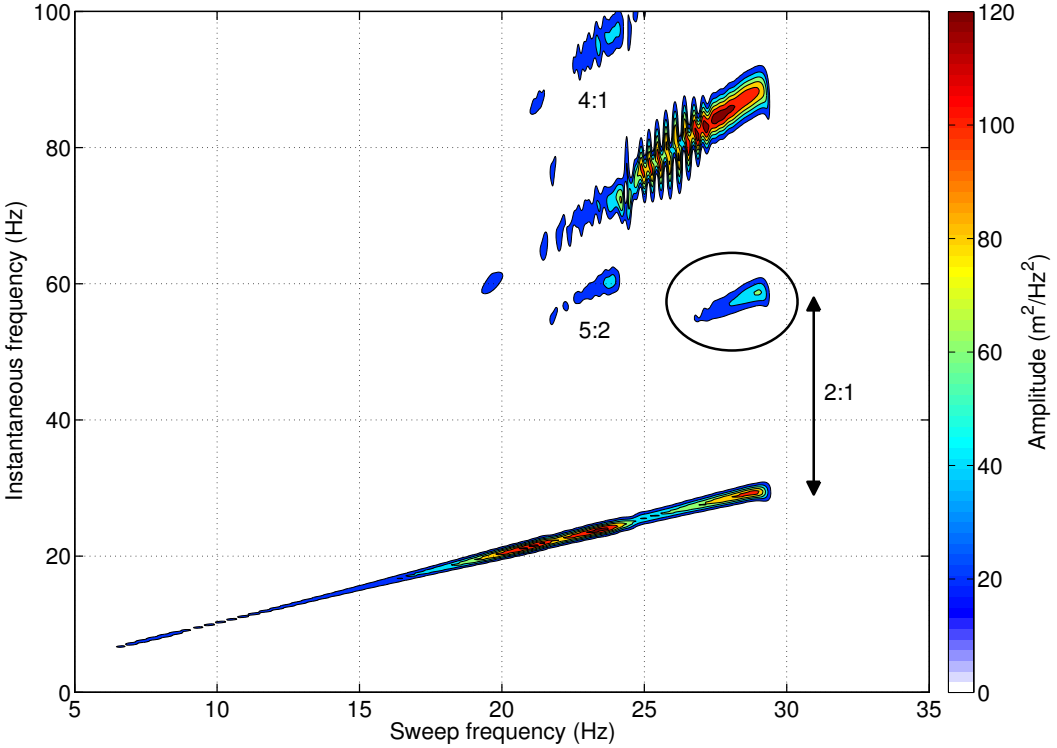

(a)

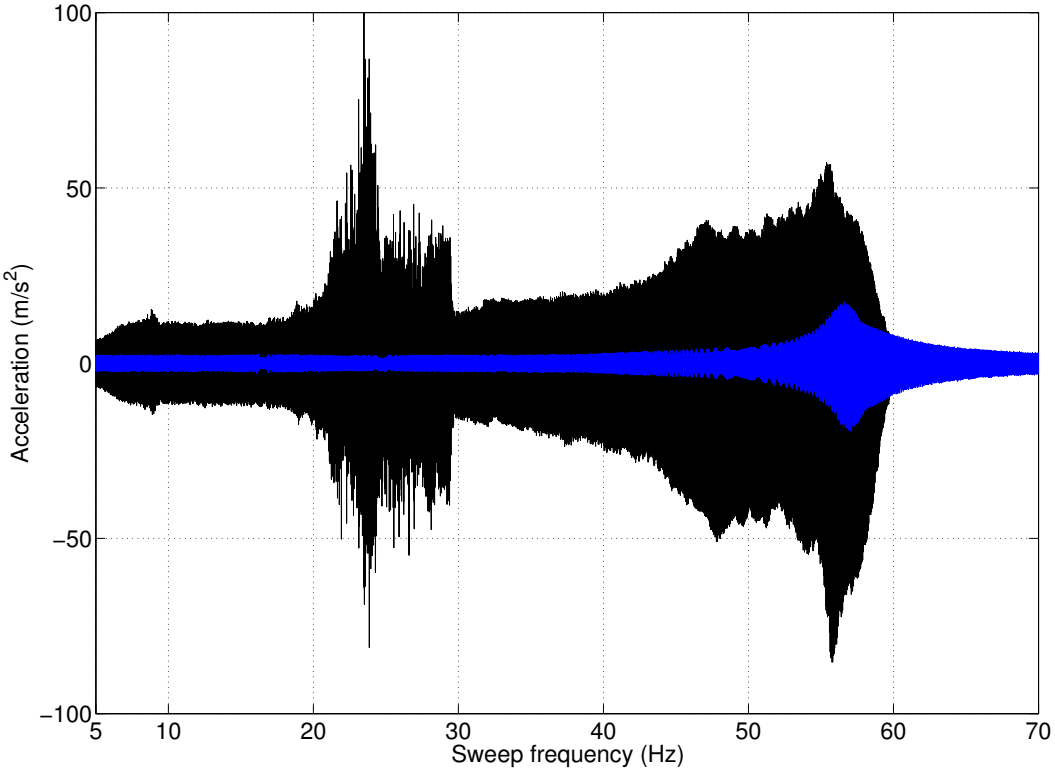

(b)

Figure 12: (a) Evidence of nonlinear modal interactions using the WT calculated at NC 4 in the Z direction, and presented in 5 – 35 Hz in linear scaling. A 2:1 modal interaction between modes 3 and 7 is encircled; (b) confirmation of the existence of the 2:1 modal interaction through the raw acceleration measured at the center of the instrument panel at 0.1 g (in blue) and 1 g (in black).

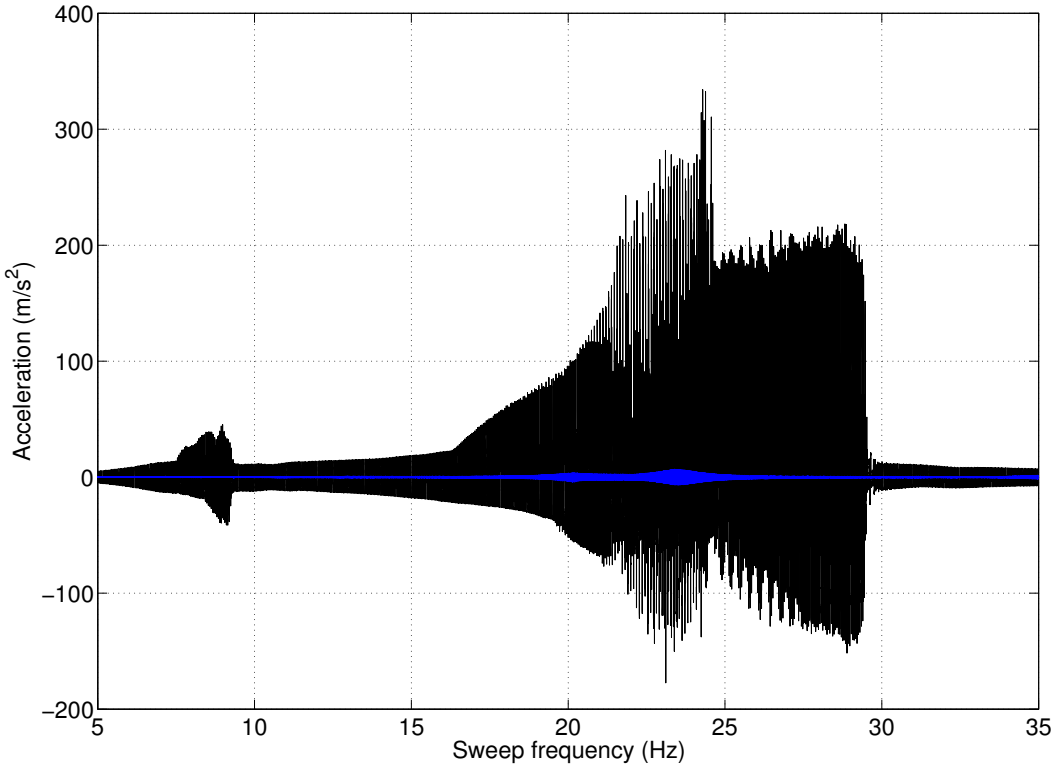

Figure 13: Acceleration measured at NC 3 at 0.1 g (in blue) and 1 g (in black).

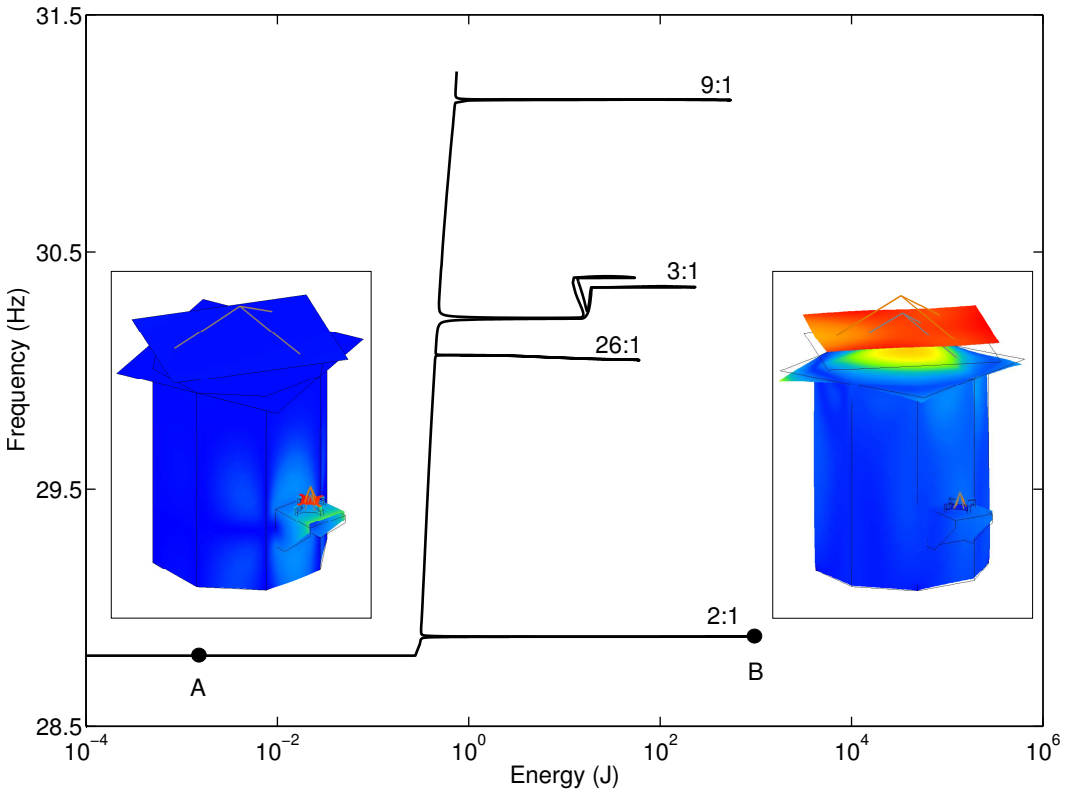

Figure 14: FEP of mode 3 computed using a continuation algorithm. The energy transfer between modes 3 and 7 is made visible through the mode shapes depicted at low level (A) and at the tip of the resonance tongue (B).

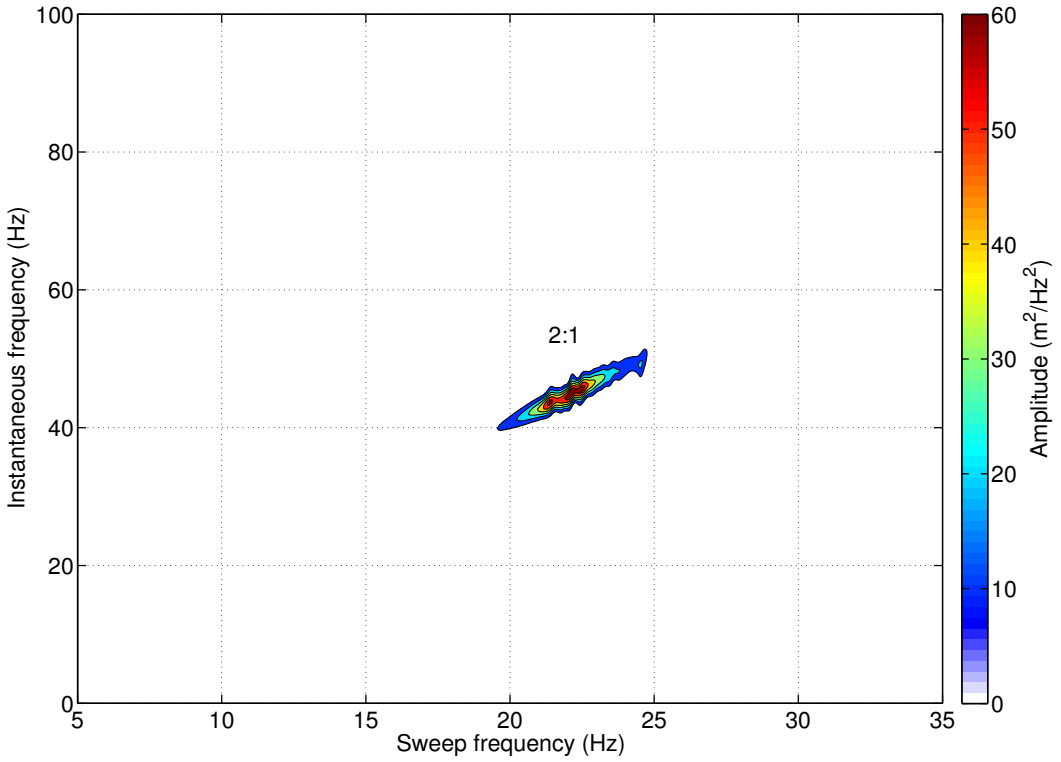

Figure 15: Evidence of another nonlinear modal interactions using the WT at NC 4 in the Y direction, presented in 5 – 35 Hz in linear scaling.

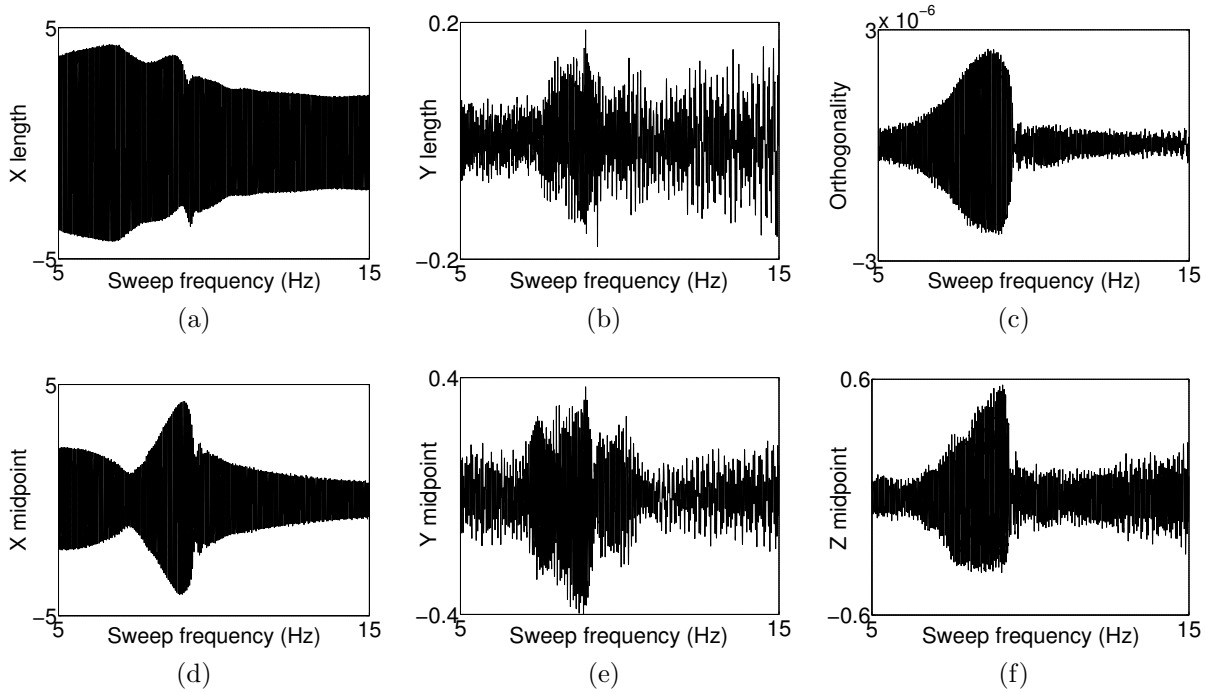

Figure 16: Verification of the geometrical conditions of rigidity at 1 g (in percent). (a – b) Length invariability; (c) orthogonality; (d – f) midpoint coincidence.

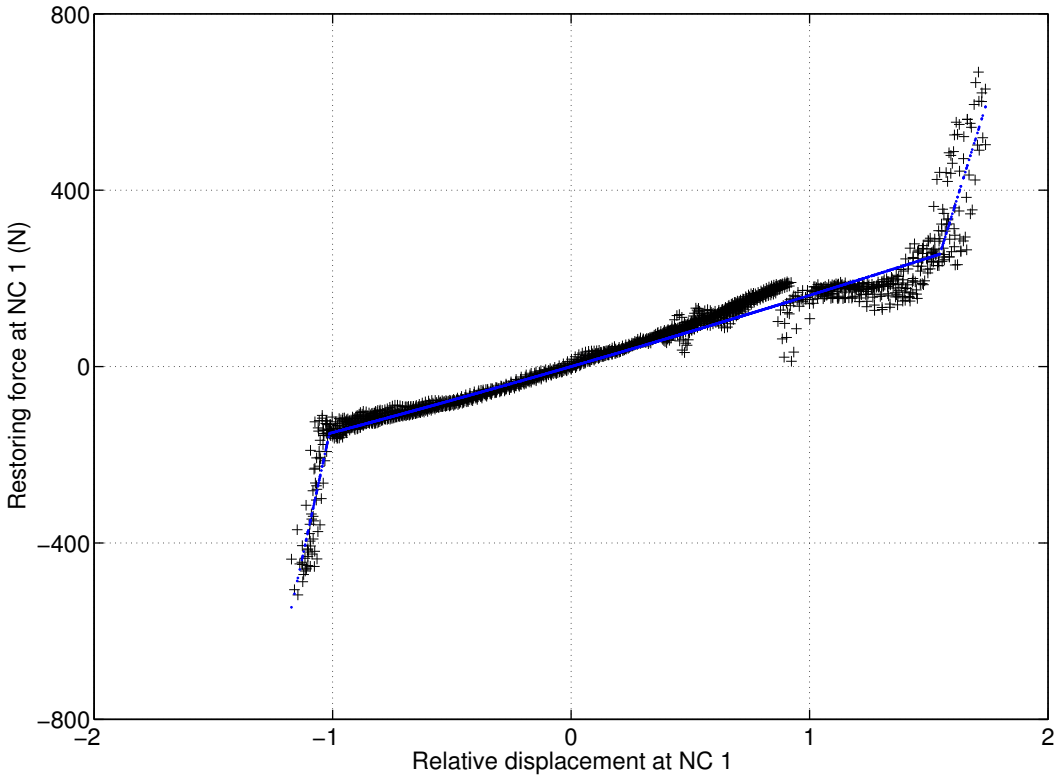

(a)

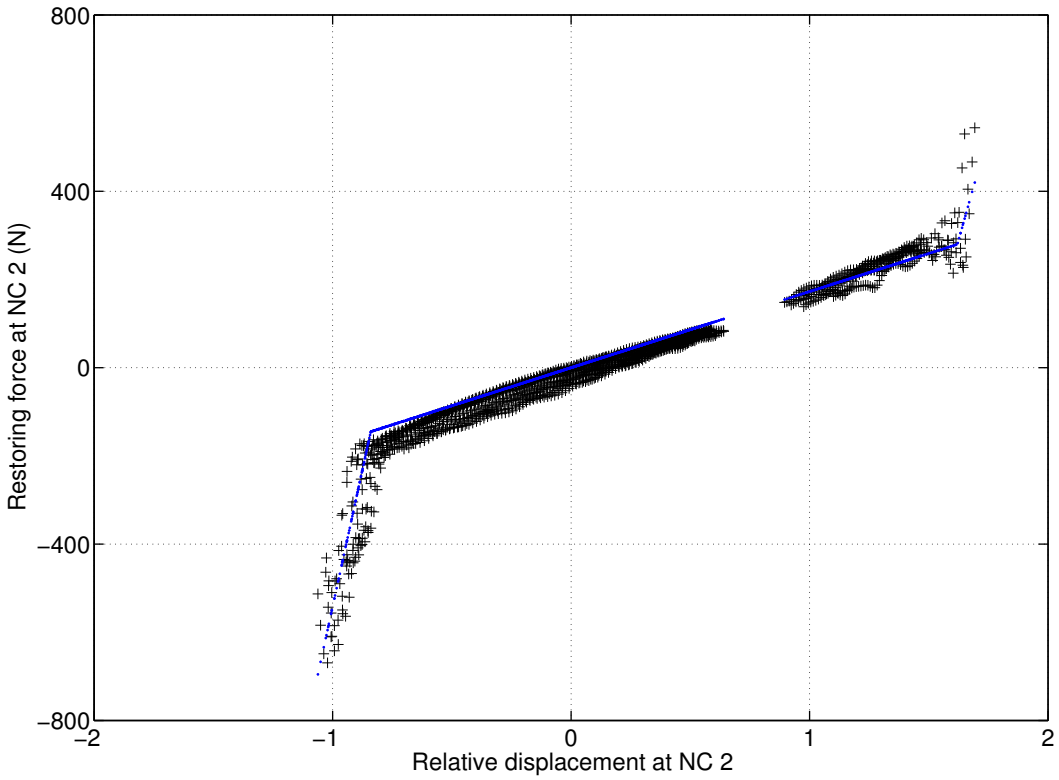

(b)

Figure 17: WEMS nonlinear stiffness curves constructed based upon Equation (12) (in black) and compared with the fitted trilinear models (in blue). (a) NC 1; (b) NC 2.

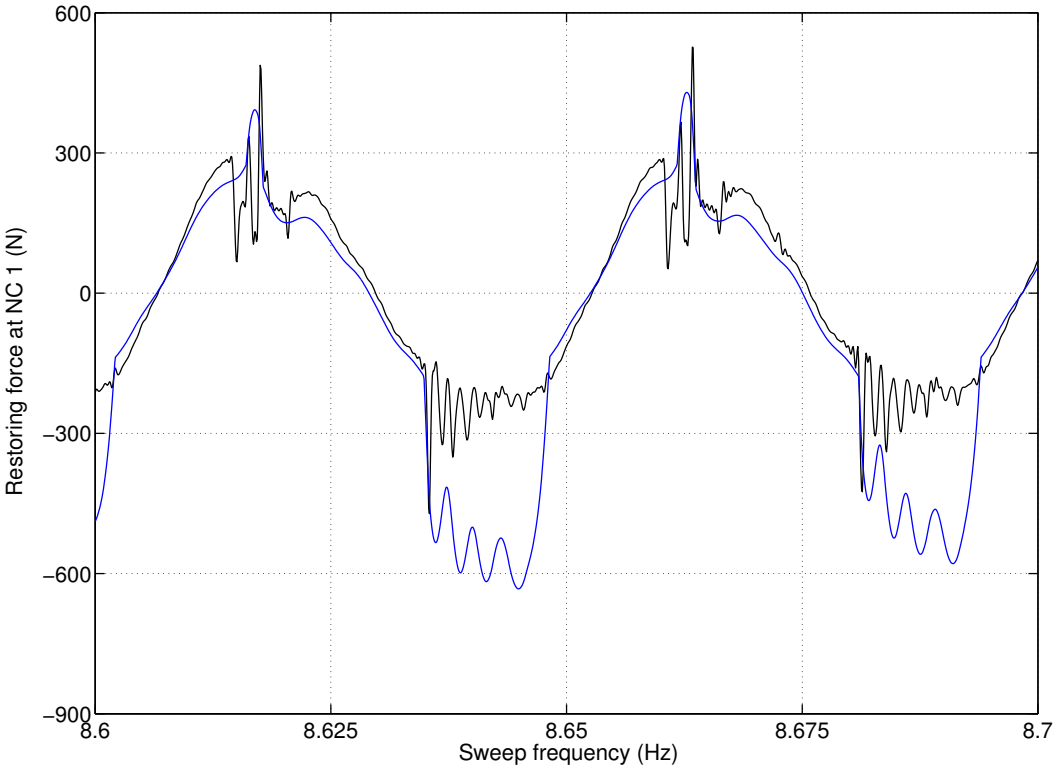

(a)

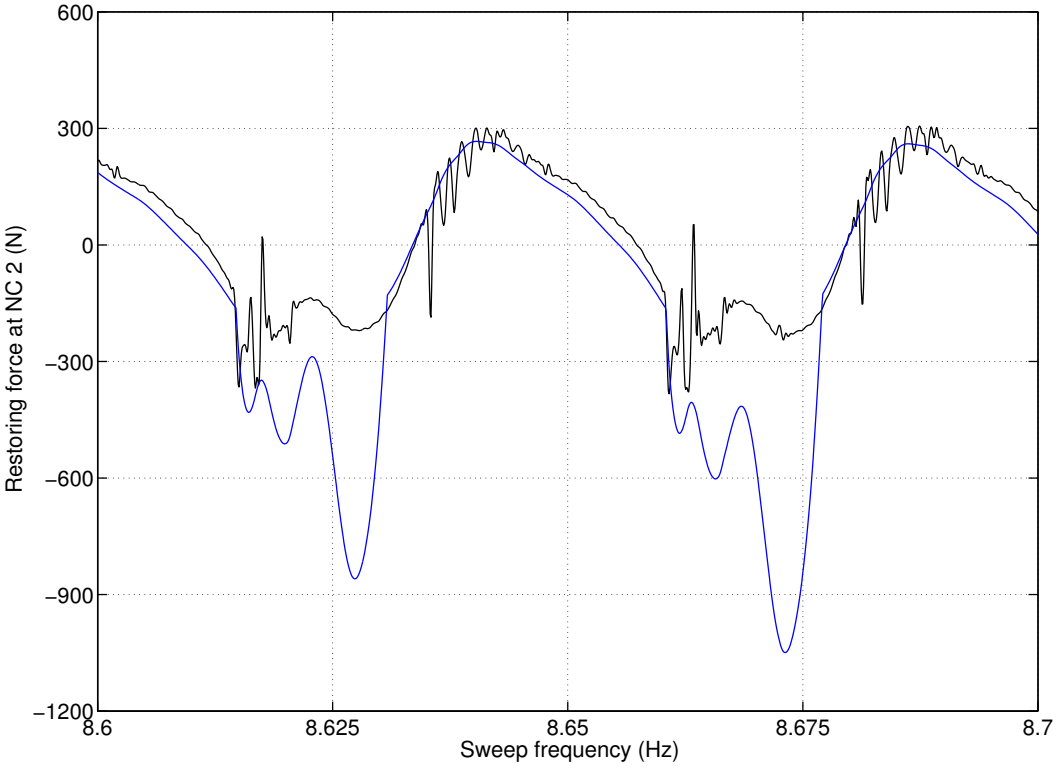

(b)

Figure 18: Comparison between the measured (in black) and reconstructed (in blue) restoring forces versus sweep frequency. (a) NC 1; (b) NC 2.

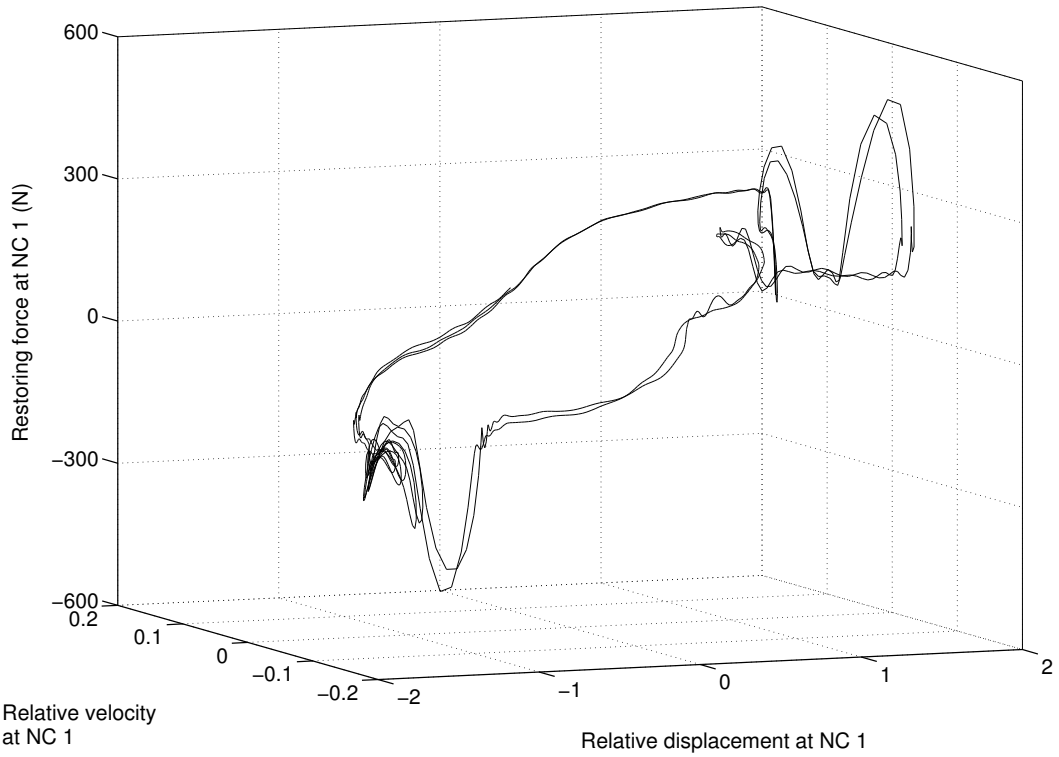

Figure 19: Restoring force surface measured at NC 1, and associated with the stiffness curve displayed in Figure 17 (a).

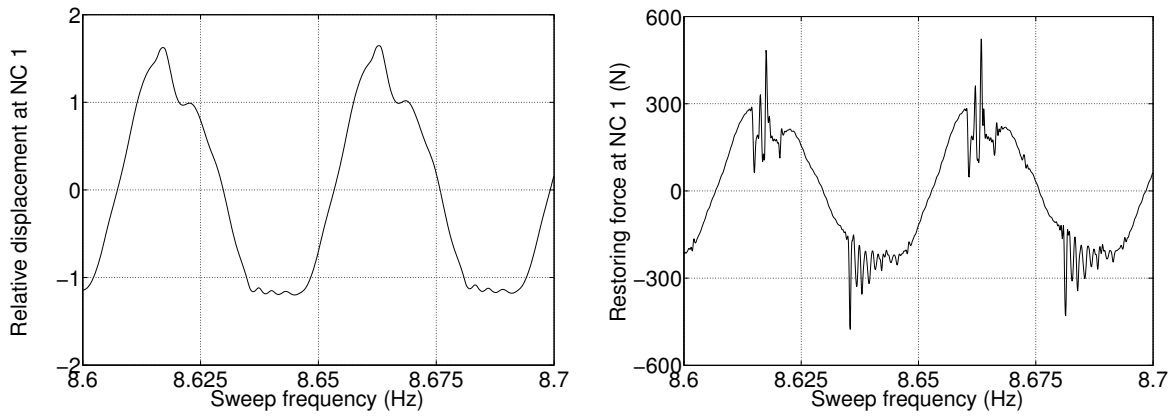

(a) (b)

Figure 20: Internal force relaxation and chattering evidenced through the comparison of the (a) relative displacement and (b) restoring force at NC 1 plotted versus sweep frequency.

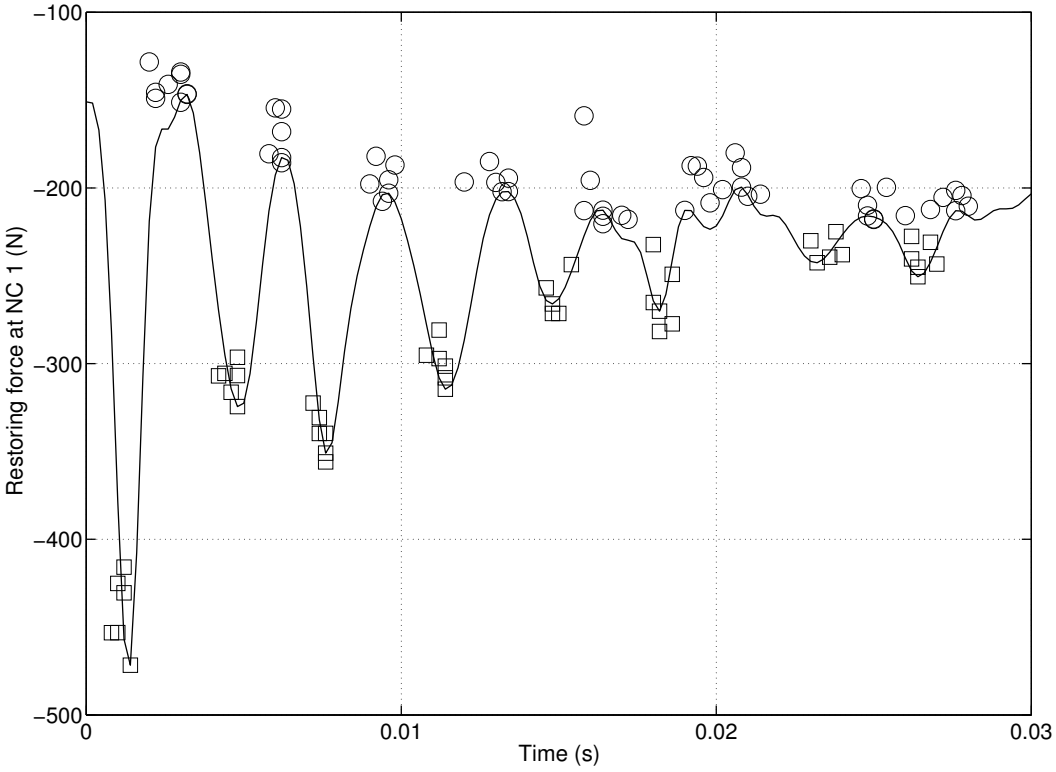

Figure 21: Locus of the minima and maxima of the oscillating force decays for 6 successive relaxation regions depicted through squares and circles, respectively. A typical force relaxation pattern is also superimposed to the clusters of minima and maxima.

List of Tables

1 Reference stiffness and damping properties of the WEMS device estimated during experiments carried out by EADS-Astrium at subsystem level. . . . 46

2 Linear resonance frequencies and damping ratios estimated using a frequency-domain subspace identification algorithm applied to low-level random data (0.001 g^2/Hz). 47

3 Damping coefficients, stiffness coefficients and clearances of NC 1 and NC 2 estimated using the RFS method and compared with their reference values. 48

	Lateral X and Y	Axial Z
Stiffness coefficient of the elastomer plots	2	8
Stiffness coefficient of the mechanical stops	40	100
Clearance	2	1.5
Damping coefficient of the elastomer plots (Ns/m)	37	63

Table 1: Reference stiffness and damping properties of the WEMS device estimated during experiments carried out by EADS-Astrium at subsystem level.

Mode	Frequency (Hz)	Damping ratio (%)
1	8.19	4.36
2	20.18	5.21
3	22.45	6.76
4	34.30	5.03
5	43.16	2.76
6	45.99	3.72
7	55.71	3.66
8	64.60	4.78
9	88.24	2.89

Table 2: Linear resonance frequencies and damping ratios estimated using a frequency-domain subspace identification algorithm applied to low-level random data (0.001 g^2/Hz).

	Reference value	NC 1	NC 2
Linear damping coefficient c (Ns/m)	63	218.29	147.75
Linear stiffness coefficient k	8	8.30	9.21
Clearance a_-	1.5	1.01	0.84
Clearance a_+	1.5	1.55	1.62
Nonlinear stiffness coefficient k_-	100	118.07	116.73
Nonlinear stiffness coefficient k_+	100	79.40	88.41

Table 3: Damping coefficients, stiffness coefficients and clearances of NC 1 and NC 2 estimated using the RFS method and compared with their reference values.